Systematic analysis of relative phase extraction in one-dimensional Bose gases interferometry

Taufiq Murtadho[*,1], Marek Gluza[1], Khatee Zathul Arifa[1,2], Sebastian Erne[3], Jörg Schmiedmayer[3], Nelly H.Y. Ng [*,1]

1 School of Physical and Mathematical Sciences, Nanyang Technological University, 639673 Singapore, Republic of Singapore
2 Department of Physics, University of Wisconsin-Madison, 53706 Madison, USA
3 Vienna Center for Quantum Science and Technology, Atominstitut, TU Wien, Stadionallee 2, 1020 Vienna, Austria
[*]fiqmurtadho@gmail.com, [*]nelly.ng@ntu.edu.sg

October 14, 2024

Abstract

Interference upon free expansion gives access to the relative phase between two interfering matter waves. In 1D systems, such measurements can be used to reconstruct the spatially-resolved relative phase, which is a key observable in many quantum simulations of quantum field theory and non-equilibrium experiments. However, longitudinal dynamics is typically ignored in the analysis of experimental data. In our work, we give a detailed account of various effects and corrections that occur in finite temperatures due to longitudinal expansion. We provide an analytical formula showing a correction to the readout of the relative phase due to longitudinal expansion and mixing with the common phase. Furthermore, we numerically assess the error propagation to the estimation of the gases' physical quantities such as correlation functions and temperature. We also incorporate systematic errors arising from experimental imaging devices. Our work characterizes the reliability and robustness of interferometric measurements, directing us to the improvement of existing phase extraction methods necessary to observe new physical phenomena in cold-atomic quantum simulators.

Contents

1   Introduction

Matter-wave interference [1] not only highlights the quantum nature of matter but also provides ultra precise sensors for metrology and serves as a sensitive probe for the intricate many body physics of ultracold quantum gases and quantum simulators [2]. A key technique thereby is time-of-flight (TOF) measurements, where the quantum gas expands upon being released from the trap. If two such expanded clouds overlap, they form a matter-wave interference pattern from which the relative phase between the trapped clouds can be extracted. If the expansion preserves local information, properties connected to the relative local phase in the original samples can be extracted.

This rational was extensively used in particular for 1D cold-atomic quantum field simulators to study non-equilibrium dynamics [3], prethermalization [4, 5], area law scaling of the mutual information [6], and quantum thermodynamics [7, 8]. This is because the statistical properties of relative phases [9] can be used to infer physical quantities of the gas such as temperature [10], relaxation time scales [11, 12]; the nature of excitations through full distribution functions [13, 14] and quantum tomography [15]; the quantum field theory description through correlation functions [16, 17]; and the propagation of information [18, 19]. In all these investigations, measuring interference in time of flight and then inferring the *local* relative phase and its fluctuations and correlations is an essential tool.

In this work, we perform a focused study on the TOF measurement of two parallel 1D Bose gases, going beyond the initial idealized reasoning in [20, 21]. We systematically address a variety of different physical phenomena that can modify the interference patterns and thereby the extraction of the local relative phase. We assess the accuracy of the *decoding*, i.e. the inference of the relative phase in the trapped clouds from the observed interference. Such a detailed and systematic analysis of the various effects that can influence TOF measurement becomes indispensable when pushing further the detailed analysis of low dimensional many body quantum systems and the quantum field simulators they enable.

To reliably extract the relative phase, we need an accurate understanding of the measurement dynamics. If the trap is switched off rapidly, the dynamics are well approximated by a quench into free evolution [20, 21], which leads to the gas expanding ballistically while free falling. For 1D systems, such free expansion can be divided into expansion in the transversal directions (perpendicular to the length of the gas) and longitudinal direction (along the length of the gas). Although previous studies [22, 23] often neglect longitudinal expansion, recent theoretical works have started to address its significance [21, 24, 25]. In particular, they unveil new phenomena affecting the formation of interference patterns such as density ripples [20], and mixing with common (symmetric) phases [21, 24]. A natural question then arises: How do these factors influence the relative phase extraction fidelity and the determination of gases' physical properties? To the best of our knowledge, no systematic answer has been offered in
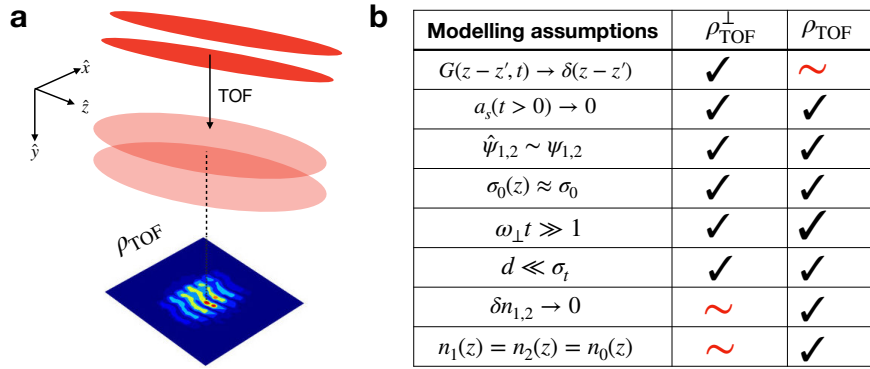
Figure 1: (**a**) The setup schematics for relative phase measurement of parallel quasi-one dimensional Bose gases (red) after time of flight (TOF) adapted from Ref. [26] (**b**) Comparison table for the assumptions used to derive different models for TOF density [Eqs. (4)-(5)]. The $\sim$ symbol means that the assumption can be relaxed in general.

the literature. This paper therefore aims to comprehensively address this question.

The paper is structured as follows: after this brief introduction, we summarize the developments in modelling TOF measurement dynamics for parallel 1D systems in Sec. 2. In Sec. 3 we develop a perturbative theory for incorporating longitudinal dynamics, and derive analytical expressions for the systematic readout errors in the extracted phase. Sec. 4 provide numerical analyses to assess the influence of errors on the estimation of the various physical quantities of the gases, accounting for modelling errors (Sec. 4). We conclude with a brief discussion and outlook in Sec. 6.

2 Free expansion dynamics of parallel 1D Bose gases

We consider a pair of parallel one-dimensional bosonic gases of length L extending along the z-axis (longitudinal axis) and separated by a distance d along one of the transversal axes, e.g. the x-axis [Fig. 1a]. Let $\hat{\psi}_j(z)$ be the bosonic annihilation operator with subscripts $j = 1, 2$ indexing the left and right well respectively. This operator can be decomposed as $\hat{\psi}_j(z) = e^{i\hat{\phi}_j}\sqrt{\hat{n}_j}$ with $\hat{n}_j$ and $\hat{\phi}_j$ being the density and phase operators. In this paper, we will use the semiclassical approximation by replacing $\hat{\psi}_j(z)$ with a scalar field $\psi_j(z) = e^{i\phi_j(z)}\sqrt{n_j(z) + \delta n_j(z)}$ where $n_j(z)$ is the mean density, and $\delta n_j(z), \phi_j(z)$ are density and phase fluctuations respectively. The objective of 1D Bose gases interferometry is to measure the relative phase fluctuation $\phi_-(z) = \phi_2(z) - \phi_1(z)$. This can be achieved through TOF scheme, whereby the atomic cloud is imaged after being released and expanded for some time t. The image encodes information about the in-situ phase fluctuations in the resulting interference pattern of the expanded density measured in experiments.

In the following, we assume the system to be initially in the quasi-1D regime, i.e. only occupying the Gaussian transverse ground state wavefunction [22, 27, 28]

$$\Psi_j(x, y, z, 0) = \frac{1}{\sqrt{\pi\sigma_0^2(z)}} \exp\left(-\frac{(x \pm d/2)^2 + y^2}{2\sigma_0(z)^2}\right)\psi_j(z), \qquad (1)$$

where the right and left wells are assumed to be symmetric with respect to the origin. The Gaussian width $\sigma_0^2(z) = \sigma_0^2\sqrt{1 + 2a_s n_j(z)}$ depends on the scattering length a_s, the mean den-

sity $n_j(z)$, and the single-particle ground state width $\sigma_0 = \sqrt{\hbar/(m\omega_\perp)}$ given by the atomic mass m and the transverse harmonic confinement frequency $\omega_\perp$. For the moment, we will ignore the radial broadening due to atomic repulsion such that the width $\sigma_0(z) \equiv \sigma_0$ is uniform along the condensate. We discuss the effect of scattering in Sec. 6 and Appendix E.

We model TOF expansion as a ballistic expansion, without any external potential nor any interaction (i.e. $a_s(t > 0) = 0$). The latter is justified due to the fast decrease of interaction energy as a result of the rapid expansion of the gas in the tightly confined transverse directions characterized by $\omega_\perp$. Thus, for $t > 0$ the system is effectively governed by free particle dynamics [20, 21, 25]

$$\Psi_j(\vec{r}, z, t) = \int d^2\vec{r}'\, dz'\, G(\vec{r} - \vec{r}', t) G(z - z', t)\, \Psi_j(\vec{r}', z', 0), \tag{2}$$

where $\vec{r}$ is a short-hand notation for the position vector in the transverse plane and $G(\xi, t) = \sqrt{\frac{m}{2\pi i \hbar t}} e^{-m\xi^2/2i\hbar t}$ is the free, single-particle Green's function. We also note that a recent work [25] has developed a fast and efficient method to numerically evaluate Eq. (2). In our analytical contributions, we make use of additional approximations to obtain a simplified analytical form of the time evolution. Thus, our results are complementary to that of Ref. [25], while paving the way for a further systematic understanding of the TOF scheme.

As the gases expand, they start to overlap and coherently interfere. We are interested in the density image of the atomic cloud after interference as seen from the vertical direction (y-axis), i.e.

$$\rho_{\text{TOF}}(x, z, t) = \int dy\, |\Psi_1(\vec{r}, z, t) + \Psi_2(\vec{r}, z, t)|^2. \tag{3}$$

After substituting the time-evolved fields from Eq. (2) and applying the assumptions listed in Fig. 1b, one arrives at a simplified formula for the expanded density [22, 23]

$$\rho_{\text{TOF}}^\perp(x, z, t) = A(z, t) e^{-x^2/\sigma_t^2} \Big[1 + C(z) \cos\big(kx + \phi_-(z)\big)\Big], \tag{4}$$

where $\sigma_t = \sigma_0 \sqrt{1 + \omega_\perp^2 t^2}$ is the expanded Gaussian width, $k(t) = d/(\sigma_0^2 \omega_\perp t) = md/(\hbar t)$ is inverse fringe spacing, and $A(z, t)$ and $C(z)$ are interference peaks amplitudes and contrasts respectively. In experiments, the relative phase $\phi_-(z)$ is obtained by fitting the interference image to Eq. (4), and so we refer to it as 'transversal fit formula'. The superscript $\perp$ means we have ignored longitudinal dynamics by substituting $G(z - z', t) \approx \delta(z - z')$ in Eq. (2). In addition, the formula also assumes $\omega_\perp t \gg 1$ and $d \ll \sigma_t$ such that the overlapping transverse Gaussian can be approximated as a single Gaussian centred at the origin. Furthermore, although they can be relaxed, we consider identical mean density $n_1(z) = n_2(z) = n_0(z)$ and ignore density fluctuation $\delta n_{1,2} \ll n_0$.

This work explores the impact of longitudinal expansion on the accuracy of relative phase extraction. In other words, we go beyond Eq. (4) by including longitudinal dynamics in our analysis, where the final density after expansion and interference is written as [21]

$$\rho_{\text{TOF}}(x, z, t) = A e^{-x^2/\sigma_t^2} \left| \int_{-L/2}^{L/2} dz'\, G(z - z', t) \sqrt{n_0(z')} e^{i\phi_+(z')/2} \cos\left(\frac{kx + \phi_-(z')}{2}\right) \right|^2, \tag{5}$$

where $\phi_+(z) := \phi_1(z) + \phi_2(z)$ is the common (symmetric) phase [24, 29], typically unmeasured in experiments. We provide a detailed derivation of Eq. (5) in Appendix A and we show how to recover Eq. (4) from Eq. (5) in Appendix B. The mixing with common degrees of freedom in Eq. (5) is a new phenomenon neglected in Eq. (4). Meanwhile, longitudinal expansion manifests itself through the Green's function kernel which allows local correlation
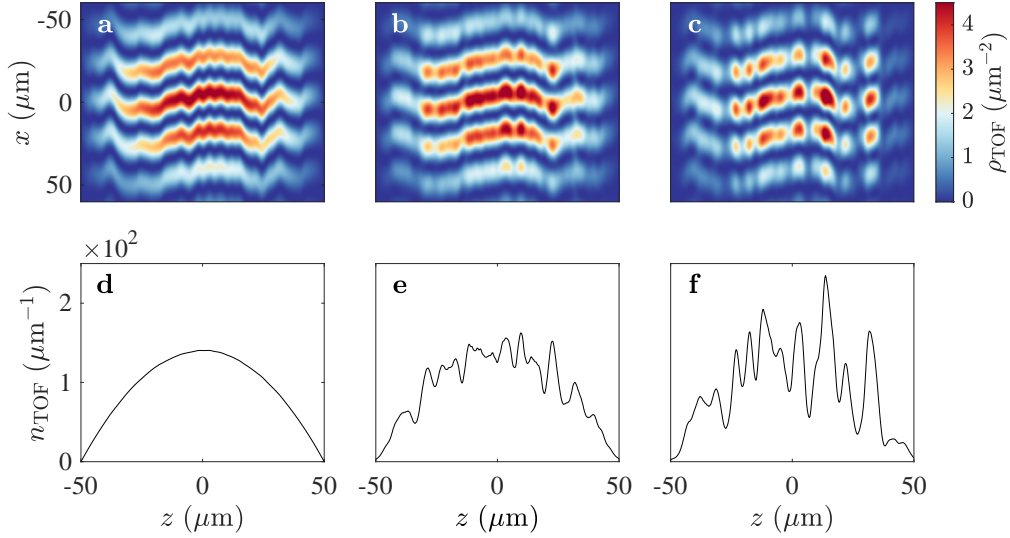
Figure 2: Comparison between three different TOF expansion models: (a) $\rho_{\text{TOF}}^{\perp}$, (b) ρ_{TOF} with $\phi_+(z) = 0$, and (c) ρ_{TOF} with $\phi_+(z) \neq 0$. Panels **d** - **f** show the respective TOF longitudinal density $n_{\text{TOF}} = \int \rho_{\text{TOF}} \, dx$. The mean insitu density $n_0(z)$ is set to follow the Thomas-Fermi approximation in harmonic potential (inverse parabola) with peak density 75 μm^{-1}. The other parameter values are $t = 15$ ms, $\omega_\perp = 2\pi \times 2$ kHz, $L = 100$ μm, $d = 3$ μm, and m is the mass of ^{87}Rb. These parameters are fixed throughout the paper unless stated otherwise.

between density at z and $z' \neq z$. We refer to Eq. (5) as the *'full expansion formula'*. Unlike the transversal fit formula, the integral form and the dependence on the common phase make it difficult to use the full expansion formula as a fit function.

We conclude our description of these models by illustrating their differences in Fig. 2a-c, showing a comparison between interference patterns of identical phase profiles computed with different expansion models. Their differences are visible through the longitudinal variation of the central peaks. They can also be seen more clearly by numerically evaluating longitudinal density $n_{\text{TOF}}(z, t) = \int dx \, \rho_{\text{TOF}}(x, z, t)$, which is directly measurable in experiments by imaging the atoms along the x-axis [10, 20, 22]. The result is shown in Figs. 2d-e with the transverse fit formula showing no density ripples [Fig. 2d], i.e. $n_{\text{TOF}}(z) = n_0(z)$, in contrast with the full formula [Figs. 2e-f].

The density ripples imply the presence of *systematic* longitudinal correlations in the interference pattern induced by free expansion, which is neglected in the transversal expansion model. Since we read out the relative phase from the interference pattern, it is natural to ask whether this density correlation will cause a systematic correlation in the readout phase as well, leading to a systematic error between *true* insitu phase and the readout phase. This error is indeed numerically reported in Ref. [21] but with no systematic characterization of their behaviour. We will discuss this in the next section.

3 Readout phase error due to longitudinal expansion

In experimental analysis, longitudinal dynamics are often ignored, and Eq. (4) is used to read out the relative phase from the density interference pattern. If we relax this assumption, the expression for the final density is given by Eq. (5), which is considerably more complicated
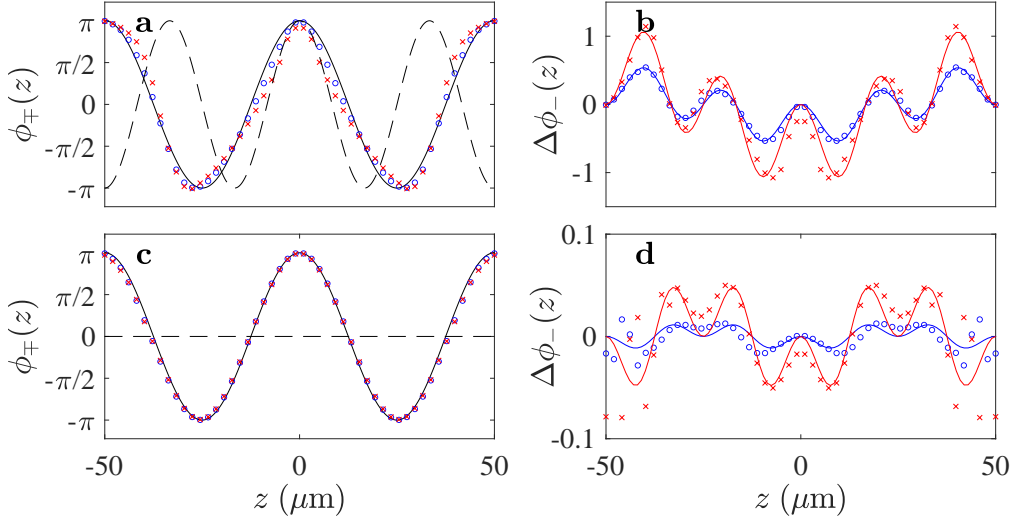
Figure 3: Simple model illustrating the different contributions of relative and common phase on the measured interference patterns in time of flight. (**a**) Input relative (solid black line) and common (dashed black line) phase profiles $\phi_-(z) = \pi \cos(4\pi z/L)$ and $\phi_+(z) = \pi \cos(6\pi z/L)$ together with the extracted phase profiles $\phi_-^{(\text{out})}(z)$ with $t = 7$ ms (blue circles) and $t = 15$ ms (red crosses). (**b**) Phase shift induced by longitudinal expansion $\Delta\phi_-(z,t) = \phi_-(z) - \phi_-^{(\text{out})}(z)$. The solid lines are fitting curves based on Eq. (9). Panels **c-d** are repetition of **a-b** with $\phi_+(z) = 0$. Numerical errors have been accounted for by subtracting the phase error using the transversal model in both encoding and decoding. The initial mean density profile is the same as in Fig. 2 (inverse parabola).

and no longer useful as a fitting function. Our aim in this section is to assess the modelling error that may arise from ignoring longitudinal expansion. We do this by treating the integral in Eq. (5) *perturbatively*.

We start by defining an integrand function,

$$I(x, z', t) \equiv \sqrt{n_0(z')} e^{i\phi_+(z')/2} \cos\left(\frac{kx + \phi_-(z')}{2}\right), \tag{6}$$

so that the integral in Eq. (5) can be written as $\int_{-L/2}^{L/2} dz' \, G(z - z', t) I(x, z', t)$. Similar the stationary phase approximation, the integrand's dominant contribution will come from $z' \approx z$. We may then perform asymptotic expansion of the integral around that point in analogy to Laplace's method [30], i.e. we perform Taylor expansion of $I(x, z', t)$ centred around z.

We show in Appendix C that up to second-order approximation, Eq. (5) can always be expressed in the following form

$$\rho_{\text{TOF}}(x, z, t) \approx A'(z, t) e^{-x^2/\sigma^2(t)} \left[1 + C'(z, t) \cos(kx + \phi_-(z) - \Delta\phi_-(z, t)) \right], \tag{7}$$

where $A'(z, t)$, $C'(z, t)$ now include corrections from longitudinal expansion. The above implies that, at least up to the second order, longitudinal expansion does not change the functional relationship between $\rho_{\text{TOF}}(x, z, t)$ and $\phi_-(z)$. This demonstrates the robustness of the transversal fit formula; nevertheless, longitudinal expansion still influences the extracted fit parameters. In particular, it introduces a *systematic phase shift* $\Delta\phi_-(z, t)$ into the readout phase, so that

$$\phi_-^{(\text{out})}(z, t) = \phi_-(z) - \Delta\phi_-(z, t). \tag{8}$$

For a uniform gas, the dominant corrections for the phase $\Delta\phi_-(z,t)$ are expressed in terms of scaled derivatives of the phases

$$\Delta\phi_-(z,t) = \frac{1}{2}(\partial_\eta\phi_-)(\partial_\eta\phi_+) + \frac{1}{8}(\partial_\eta^2\phi_-)(\partial_\eta\phi_-)^2 + O(\partial_\eta^4), \tag{9}$$

where derivatives are taken with respect to a scaled coordinate $\eta = z/\ell_t$ with $\ell_t = \sqrt{\hbar t/m}$ being the length scale of longitudinal expansion. In the standard Bogoliubov theory for 1D gas [31], the scaled derivative of the phase with respect to a finite lattice length is considered a small parameter. Similarly, our formula is expanded with respect to small parameters $\partial_\eta\phi_\pm$ with ℓ_t being analogous to lattice length. The corrections to Eq. (9) are of order four or higher in scaled phase derivatives [see Appendix C]. We also note that the form in Eq. (9) already uses a linearization of an arctan function. When considering phase profile with high modes fluctuation, one might need to adopt the full analytical form derived in Appendix C.

Equations (7)-(9) are the main analytical results of this paper. In particular, Eq. (9) is useful to assess the reliability of the existing phase readout protocol. For example, it shows that the readout error grows with a longer expansion time. This is intuitive since a longer longitudinal expansion time would lead to a more systematic longitudinal correlation spread along the gas. Moreover, Eq. (9) also clearly shows a dominant phase shift correction due to mixing with the common phase, which was previously unnoticed. We also find a higher-order correction that depends only on the derivatives of the relative phase, signifying a systematic error purely due to the presence of longitudinal Green's function.

We compare our analytical prediction with numerical data by encoding smooth phase profiles, e.g. $\phi_-(z) = \pi\cos(4\pi z/L)$ and $\phi_+(z) = \pi\cos(6\pi z/L)$, into density interference pattern computed with the *full expansion formula* and then decode the relative phase with the *transverse fit formula*. We find agreement between numerical data and our analytical prediction up to finite size effects near the boundary [Fig. 3]. We also examined the fit for various other smooth profiles and obtained similar results. Note that the numerical data does not assume uniform density and yet Eq. (9) fits the data quite well, demonstrating the usefulness of our formula in realistic scenarios where density varies sufficiently slowly.

4   Reconstruction of physical quantities

Ultimately, we are interested in reconstructing physical quantities associated with the gas' initial state, which we assume to be given by a Hamiltonian of the form [20, 32, 33]

$$H = H_{TLL}(\delta\rho_+, \phi_+) + H_{TLL}(\delta\rho_-, \phi_-) - 2\hbar J n_0 \int dz\, \cos\phi_-(z)\,, \tag{10}$$

where H_{TLL} is the Tomonaga-Luttinger liquid Hamiltonian

$$H_{TLL} = \int dz \left[\frac{\hbar^2 n_0(z)}{4m}(\partial_z\phi(z))^2 + g\,(\delta\rho(z))^2 \right]. \tag{11}$$

While the common mode is determined by this Gaussian theory, the non-Gaussianity of the relative degrees of freedom can be experimentally tuned via the single particle tunnelling strength J, giving rise to the sine-Gordon model. The relevance of the cosine potential can be characterized by $q = \lambda_T/l_J$ which is directly related to the experimentally accessible coherence factor $\langle\cos(\phi_-)\rangle$. The thermal coherence length $\lambda_T = \hbar^2 n_{1D}/(mk_B T)$ for uniform gas $n_0 = n_{1D}$ and phase locking length $l_J = \frac{1}{2}\sqrt{\hbar/mJ}$ determine the randomization and restoration of the phase due to temperature and tunnel coupling respectively. In thermal equilibrium
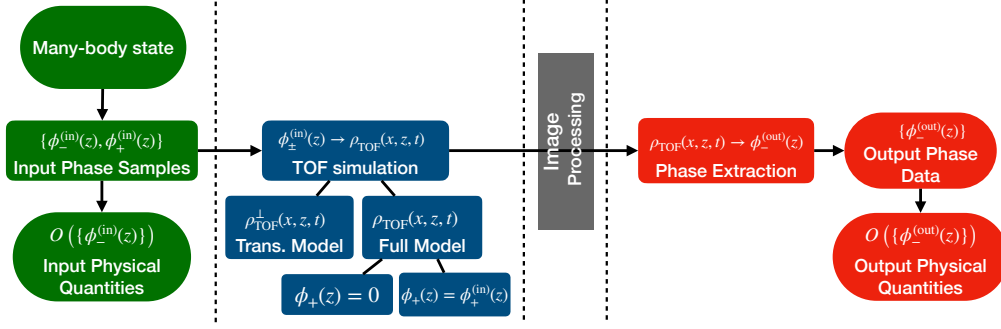
Figure 4: The simulation workflow is divided into four stages, separated by the dotted lines. The first stage (green boxes) represents the input to the simulation, obtained by sampling relative and common phase profiles from an input state. The next stage (blue boxes) represents TOF encoding implemented with three different models. The last stage (red boxes) represents decoding where relative phases and physical quantities are inferred by fitting with the transverse fit formula (4). The goal of the simulation is to compare the input and output physical quantities.

phase correlation functions for varying q, i.e. strength of the tunnel coupling J, have been experimentally computed up to the 10th order [32] and found in agreement with predictions of the sine-Gordon model.

In this section, we assess the reliability of TOF measurement for such a task, especially in the light of possible error propagation from $\Delta\phi_-(z,t)$. We begin with investigating the reconstruction of physical quantities associated with uncoupled Luttinger liquid ($J = 0$) in thermal equilibrium in Subsecs. 4.1-4.4. We then discuss the TOF reconstruction of second-order and fourth-order correlations of the coupled sine-Gordon theory in the Gaussian ($q = 0.5$) and non-Gaussian regime ($q = 3$) in Subsec. 4.5. From here onwards, we mainly resort to numerical simulation, where our workflow is summarized in Fig. 4. The code used to perform the simulation is available in Ref. [34].

- **Independent sampling of relative and common phase profiles.** We sample many instances of $\{\phi_\mp^{(\text{in})}(z)\}$ from a many body state. In our case, the many body state would either be a thermal Gaussian state or a non-Gaussian sine-Gordon state. The phase profiles corresponding to thermal Gaussian state are sampled from a multivariate normal distribution following a thermal covariance matrix [15], with small tunnelling $J = 0.1$ Hz to renormalize the zero modes. Meanwhile, the non-Gaussian phase profiles are sampled by a stochastic process described by an Itô equation [35, 36].

  The sampled phase profiles are the input to our simulation. Using these inputs, the ground-truth physical quantities $\mathcal{O}\left(\left\{\phi_-^{(\text{in})}(z)\right\}\right)$ can be computed. Although it may contain statistical fluctuations, given sufficiently many samples of the phase profiles, the computed quantities $\mathcal{O}$ should closely match their theoretical values.

- **Simulation of the TOF encoding of phases into density interference patterns.** Given the phase profiles, we simulate TOF by computing density after TOF (ρ_{TOF}) using Eq. (5) with varying expansion time t. To control for the influence of common phases, we perform the simulation twice for every t, once with zero common phase ($\phi_+(z) = 0$) and the second time with the sampled common phase ($\phi_+(z) = \phi_+^{(\text{in})}(z)$). In addition, we simulate the transverse expansion model to control for numerical error in the relative phase decoding process (explained below).

- **Decoding the relative phase from interference patterns.** With the obtained ρ_{TOF}, we
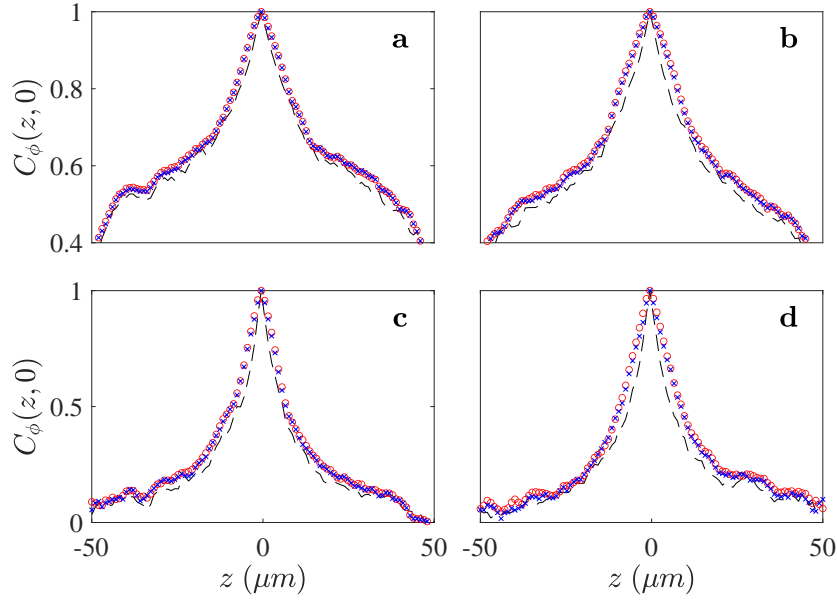
Figure 5: The input (dashed black line) and output two-point phase correlation function $C_\phi(z,0)$ for $T_- = 25$ nK (**a-b**) and $T_- = 75$ nK (**c** - **d**) reconstructed with 500 TOF simulations. The first (**a**, **c**) and second (**b**, **d**) columns are reconstructed with 7 ms and 15 ms, respectively. The blue crosses (red circles) are data from TOF simulation with $\phi_+(z) \neq 0$ ($\phi_+(z) = 0$) sampled from the same thermal distribution as the relative phase ($T_+ = T_-$).

use Eq. (4) as a fitting function to extract $\phi_-(z)$. To do so, we solve a constrained optimization $\phi_-^{(out)}(z) \in [-2\pi, 2\pi]$ problem using the interior-point algorithm. We initialize the optimizer by feeding a linear function $\phi_-^{(0)}(z) = -kx_{max}$ where x_{max} is the transversal peak position at fixed z [Appendix D]. Due to phase multiplicity over a 2π period, we sometimes observe phase jumps (discontinuity) in the optimization output. We eliminate the discontinuity by applying a *phase unwrapping* protocol: adding a multiple of 2π to the phase whenever detecting a jump larger than π until discontinuity is eliminated. However, this protocol is inaccurate for highly fluctuating profiles in finite resolution, which puts a limit on the temperatures for which our method performs reliably.

After obtaining all the decoded phases data $\{\phi_-^{(out)}(z)\}$, we compute the inferred physical quantities $\mathcal{O}(\{\phi_-^{(out)}(z)\})$ and compare them to the input $\mathcal{O}(\{\phi_-^{(in)}(z)\})$ in different scenarios. Note that in Fig. 4, there is an additional image processing stage between the encoding and decoding process. This is the stage where the initial interference pattern gets modified due to the experimental setup and limitations of the imaging devices. We will momentarily ignore this stage and revisit it in Sec. 5.

4.1 Two-point phase correlation function

We first consider the two-point phase correlation function

$$C_\phi(z, z') = \langle \cos[\phi_-(z) - \phi_-(z')] \rangle \tag{12}$$

where $\langle . \rangle$ denotes average over realizations. This quantity can be evaluated analytically [37] for Gaussian theory with quadratic Hamiltonian, and has been measured in experiments to

observe light cone of thermal correlation [4] as well as recurrences [38] in parallel 1D Bose gases. Here, we will only consider a middle cut $C_\phi(z, 0)$. The comparisons between input and reconstructed $C_\phi(z, 0)$ for different parameters are shown in Fig. 5. We find that the reconstruction of phase correlation function C_ϕ is robust against systematic phase shift due to TOF. In other words, $\Delta\phi_-$, both with and without the common phase do not significantly influence the reconstruction of C_ϕ. This is intuitive since C_ϕ mostly rely on the low mode and long wavelength physics which do not get significantly influenced by $\Delta\phi_-$.

4.2 Full distribution function

Shot-to-shot variations of the interference patterns for pairs of independently created one-dimensional Bose condensates can reveal signatures of quantum fluctuation. In Ref. [13], they show that a key quantity to observe quantum fluctuation in this system is the *full distribution function* $P(\xi)$ where

$$\xi(l) = \frac{\left|\int_{-l/2}^{l/2} e^{i\phi_-(z)}\, dz\right|^2}{\left\langle\left|\int_{-l/2}^{l/2} e^{i\phi_-(z)}\, dz\right|^2\right\rangle}, \tag{13}$$

with l being a variable distance from 0 to L. We are interested in calculating the probability distribution $P(\xi)$ for different length scales l. Both theoretically and experimentally, it was observed that for a length scale comparable to the total gas length $\ell \sim L$, the distribution $P(\xi)$ is dominated by thermal fluctuations while for shorter lengths, $P(\xi)$ provides unambiguous signatures of quantum fluctuations [13]. This quantity is also used to study prethermalization of 1D Bose gases after coherent splitting [26, 39, 40].

We compare the input and reconstructed (output) full distribution function $P(\xi)$ for three different length scales in Fig. 6. We find that except for a minor reduction in the high-contrast probability, the qualitative features of the input and output distribution almost coincide. The suppression of the high-contrast probability implies that, as expansion time becomes longer, the medium contrast becomes over-represented and so it could slightly modify the skewness of the underlying distribution. We believe this is due to additional fluctuation coming from the systematic phase shift $\Delta\phi_-(z, t)$ which grows with expansion time. Furthermore, by comparing the first and second rows in Fig. 6, we also show that the common phase does not significantly influence the full distribution function. Overall, we observe the same quantum to thermal distribution transition as reported in Ref. [13]. Thus, longitudinal expansion and common phase do not play significant roles here and the existing phase readout protocol can faithfully reproduce the full distribution function function $P(\xi)$.

4.3 Velocity-velocity correlation

The spatial derivative of phase has a physical meaning as a velocity field $u_\pm(z) = (\hbar/m)\partial_z\phi_\pm(z)$ in the hydrodynamics description of cold Bosonic gas. Here, we specifically look at the correlation in the relative velocities

$$C_u(z, z') = \langle\partial_z\phi_-(z)\partial_{z'}\phi_-(z')\rangle - \langle\partial_z\phi_-(z)\rangle\langle\partial_{z'}\phi_-(z')\rangle. \tag{14}$$

If the relative velocities of the atoms at z and z' are independent, then $C_u(z, z')$ vanishes. Any non-zero values (discounting statistical fluctuation) for this quantity reflect a correlation in the relative velocities, i.e. if $C_u(z, z') > 0$ the relative velocities of the atoms at z and z' tend to align whereas if $C_u(z, z') < 0$ they tend to be opposite. Recently, the velocity-velocity correlation has been measured in experiments to observe curved light cones in a cold-atomic
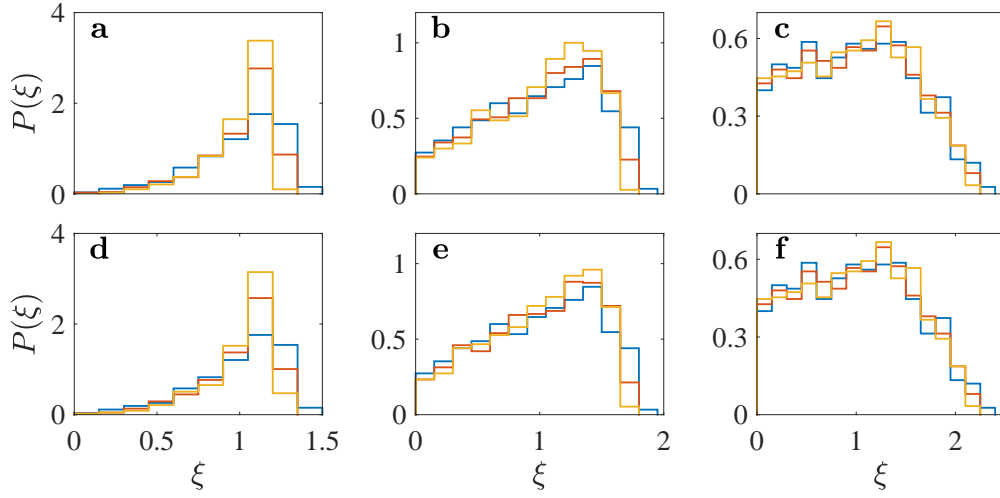
Figure 6: Full distribution function $P(\xi)$ computed with 1000 phase profiles sampled from a thermal state with $T_{\pm} = 75$ nK. The top (bottom) row **a-c** (**d-f**) corresponds to the case where $\phi_+(z) = 0$ ($\phi_+(z) \neq 0$). The length scales are $l = 9.8\ \mu$m (**a,d**), $l = 25.5\ \mu$m (**b,e**), and $l = 49\ \mu$m (**c,f**). The blue histogram is the input, red (yellow) histogram is the reconstructed distribution from 7 ms (15 ms) full expansion.
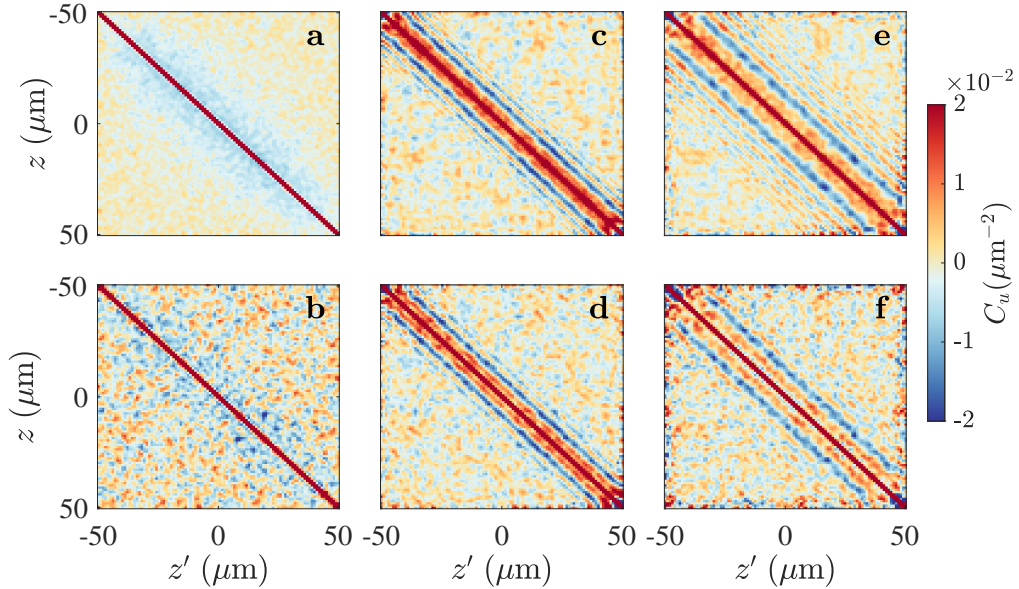

Figure 7: Velocity-velocity correlation $C_u(z, z')$ calculated from (**a**) input phase profiles and (**b**) extracted profiles with 7 ms transversal expansion (**c**) 7 ms full expansion with $\phi_+(z) = 0$ and (**d**) $\phi_+(z) \neq 0$. Panels (**e**)-(**f**) are the same as (**c**)-(**d**) except for $t = 15$ ms. Panel (**a**) is generated with 10^4 phase profiles whereas panels (**b**)-(**f**) are generated with 500 TOF simulation. The upper bound of the color bar has been adjusted to low values to accentuate structures in the off-diagonals. The input phase profiles are sampled from a thermal distribution with temperatures $T_{\pm} = 75$ nK.
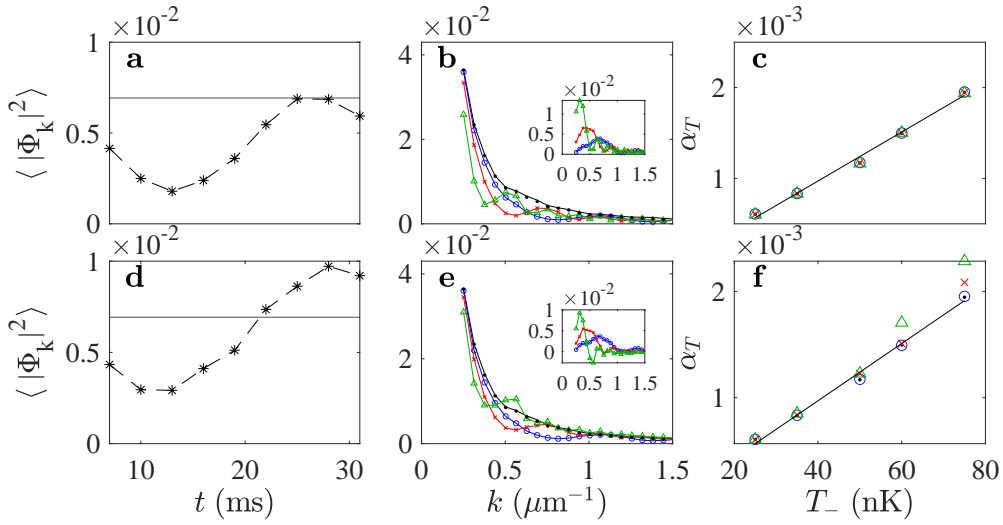
Figure 8: Thermal ($T_- = 50$ nK) mean occupation number $\langle |\Phi_k|^2 \rangle$ computed using 200 realizations of TOF measurement simulation. In panel **a**, $k = 20\pi/L$ ($\approx 0.63~\mu\text{m}^{-1}$) is fixed but expansion time is varied. In panel **b**, k is varied but expansion times are fixed at different values: $t = 7$ ms (blue circles), $t = 15$ ms (red crosses), and $t = 30$ ms (green triangles). The black solid lines are the ground truths computed from the input data. To emphasize the oscillation in the intermediate mode, we only plot data points with $k \geq 10\pi/L \approx 0.31~\mu\text{m}^{-1}$. The inset shows the residue $\Delta_k = \langle |\Phi_k^{(\text{in})}|^2 \rangle - \langle |\Phi_k^{(\text{out})}|^2 \rangle$. Panel **c** shows inverse thermal coherence length α_T as a function of temperature T_-. Panels **d-f** are the repetition of **a-c** but include common phase with temperature $T_+ = T_-$.

quantum field simulator [19]. We compare the input and output velocity correlation in Fig. 7. The in situ velocity correlation $C_u^{(\text{in})}(z, z')$ for a thermal state is not completely diagonal. Instead, it has a weak and short-distance anti-correlation as shown by Fig. 7a.

Interestingly, we observe spatial propagation of the initial anti-correlation in the TOF model with longitudinal expansion shown in Figs. 7c-d and Figs. 7e-f, which does not appear in the control simulation with only transversal expansion [Fig. 7b]. We observe the length scale for this correlation (the span of the off-diagonal) increases with a longer expansion time. Such propagation of correlation can be physically understood in a quasi-particle picture, where neighbouring quasi-particles with initial opposite velocity correlation will move further away from each other as the gas expands longitudinally. We also observe alternating patterns of positive and negative correlation which indicates momentum interference in the longitudinal direction [Fig. 7e]. However, this long-distance correlation and anti-correlation are randomized when common phases are involved and only the propagation of the primary anti-correlation persists [Fig. 7f].

This propagation is similar to what has been observed experimentally in the context of a quench from an interacting to non-interacting pair of Luttinger liquids [19]. The difference here is that we report the propagation of velocity correlation due to quenching into a free Hamiltonian induced by the TOF measurement protocol. Our results point to the necessity of calibrating the results of dynamical propagation of velocity-velocity correlation such as in Ref. [19] to the measurement background.

4.4 Mean occupation number & temperature

The mean Fourier spectrum $\langle |\Phi_k|^2 \rangle$ where $\Phi_k = (1/L) \int_{-L/2}^{L/2} e^{-ikz} \phi_-(z)\, dz$ is another relevant physical quantity of the gas, since it is related to the gas temperature T. In particular, it is directly related to the temperature of the relative sector T_-, which in general can be different from the temperature of the common sector T_+. For a uniform thermal state, their relation is given by [41]

$$\langle |\Phi_k|^2 \rangle = \frac{mk_B T}{\hbar^2 k^2 n_{1D}} = \frac{\alpha_T}{k^2}, \tag{15}$$

where $\alpha_T = 1/\lambda_T = mk_B T/(\hbar^2 n_{1D})$ is inverse thermal coherence length. By fitting $\langle |\Phi_k|^2 \rangle$ with respect to k^{-2}, we can obtain α_T and extract the temperature of the relative phase T_-. For our simulation, we will assume the relative and common degrees of freedom are in thermal equilibrium with respect to each other ($T_+ = T_-$).

We start by comparing the input and output spectrum for a thermal state with a fixed temperature $T_- = 50$ nK. We first fixed the momentum to be $k = 20\pi/L$ and varied the expansion time t. In the absence of energy transfer from other sectors, the energy in phase quadrature can not exceed its initial energy. This explains why the output spectrum appears to be upper-bounded by its in situ values [Figs. 8a,b] when common phase is absent. However, for high enough common phase temperature, the in-situ values do not provide an upper-bound anymore because initial common phase fluctuation can give extra energy to the relative phase [see Eq. (9)]. Note that in our case, energy from in situ density fluctuation is ignored.

While a perfectly faithful reconstruction of $\langle |\Phi_k|^2 \rangle$ should not depend on t, we find a non-trivial oscillation of $\langle |\Phi_k^{(\mathrm{out})}|^2 \rangle$ with respect to the expansion time attributed to longitudinal expansion [Figs. 8a,d]. This oscillation is also visible when we plot $\langle |\Phi_k|^2 \rangle$ as a function of k for different values of expansion time as shown in Figs. 8b,e. To emphasize the oscillation in the intermediate mode regime we have omitted the low-momentum population $k < 10\pi/L$. The insets in Figs. 8b,e show the residue between input and output spectrum $\Delta_k = \langle |\Phi_k^{(\mathrm{in})}|^2 \rangle - \langle |\Phi_k^{(\mathrm{out})}|^2 \rangle$, which qualitatively resembles the evolution of density ripple spectrum [20]. As expansion time gets longer, the maximum of the residue $\Delta_k^{(\mathrm{max})} = \max_k(\Delta_k)$ grows and its peak location k_{max} shifts to a lower mode.

We checked numerically that such oscillation originates from a transfer of energy from the relative phase to relative density fluctuation during the expansion. Note that although we ignore density fluctuation *in situ*, it does not prevent density fluctuation from developing as the cloud expands. Indeed, density ripples displayed in Figs. 2e-f can be considered as the common density fluctuation of the clouds after TOF. In contrast, relative density fluctuation, i.e. $\delta n_-^{(\mathrm{tof})}(z,t) = \int d^2\vec{r}\, \big[|\psi_1(\vec{r},z,t)|^2 - |\psi_2(\vec{r},z,t)|^2 \big]$ is not directly measurable in experiments, but can still be computed in simulation. We found opposite oscillatory behaviour between the spectrum of $\delta n_-^{(\mathrm{tof})}(z,t)$ and the lost energy in $\langle |\Phi_k^{(\mathrm{out})}|^2 \rangle$, giving strong evidence for energy transfer between the two fields.

Finally, we check the impact of this oscillation to the reading of temperature using Eq. (15). We perform fitting $\langle |\Phi_k|^2 \rangle = \alpha_T k^{-2}$ for different values of T_- and then plot α_T as a function of T_- shown in Figs. 8c,f. We find that the oscillation due to longitudinal expansion does not significantly affect the readout of temperatures, but the additional fluctuation from common phase does make a difference for medium to long expansion time ($t > 15$ ms) and high enough $T_+ \gtrsim 60$ nK.

4.5 Gaussian and non-Gaussian correlation functions

Equal-time higher-order correlations contain detailed information about the many body state, and can be directly calculated from the extracted phase profiles after time of flight. Computing
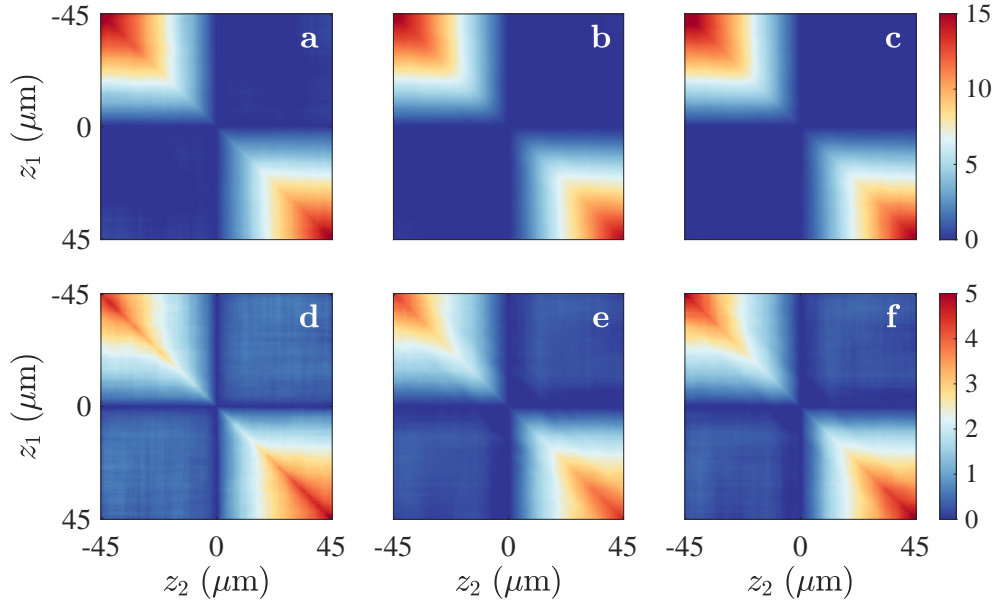
Figure 9: Second-order correlation $G^{(2)}(z_1, z_2)$ for $q \equiv \lambda_T/l_J = 0.5$ (**a** - **c**) and $q = 3$ (**d** - **f**). The first column (**a**, **d**) shows the input correlation $G_{in}^{(2)}(z_1, z_2)$, the second column (**b**, **e**) shows TOF reconstruction $G_{(out)}^{(2)}(z_1, z_2)$ with $t = 15$ ms and zero common phase $\phi_+ = 0$, and the third column includes the effect of common phase sampled from a thermal distribution with $T_+ = 75$ nK. The edge data of length 2.5 μm on each end have been omitted to suppress boundary effects.

all correlation functions is tantamount to solving a many body problem [17, 22, 32]. The N-th order relative phase correlation function referenced at $z = 0$ is defined by

$$G^{(N)}(\mathbf{z}) = \left\langle \prod_{i=1}^{N} (\phi_-(z_i) - \phi_-(0)) \right\rangle , \qquad (16)$$

where $\mathbf{z} = (z_1, z_2, ..., z_N)$. In general, the correlation function can be decomposed into the connected and disconnected part

$$G^{(N)}(\mathbf{z}) = G_{con}^{(N)}(\mathbf{z}) + G_{dis}^{(N)}(\mathbf{z}). \qquad (17)$$

The disconnected part can be expressed in terms of lower-order correlations while the connected part contains genuine new information about N-body interactions [17, 32]. The computation of correlation function of order larger than two is analytically difficult, except for special cases such as non-interacting Gaussian states, where higher-order connected correlations vanish identically for $N > 2$.

We first compare the second order correlation $G^{(2)}$ for sine-Gordon Hamiltonian in Gaussian ($q \equiv \lambda_T/l_J = 0.5$) and non-Gaussian ($q = 3$) regimes. The comparison is shown in Fig. 9. We observe only small differences between input and output correlation in the small J Gaussian regime of the sine-Gordon model, implying that TOF can faithfully reconstruct Gaussian correlation. However, in non-Gaussian regimes, we observe a spread of cross-shaped strips at the center, which can be interpreted as a correction from higher-order correlation terms induced by systematic phase shift error.

Next, we compare the input and TOF reconstruction of fourth-order correlation function $G_{con}^{(4)}(z_1, z_2, z_3, z_4)$. This quantity strictly vanishes for Gaussian states. We have checked that in
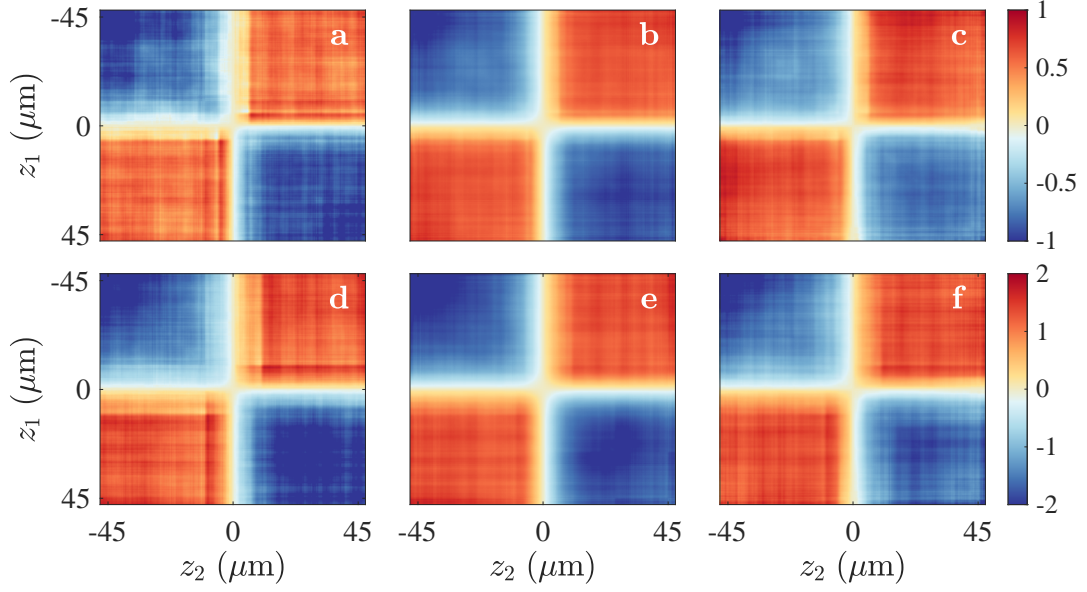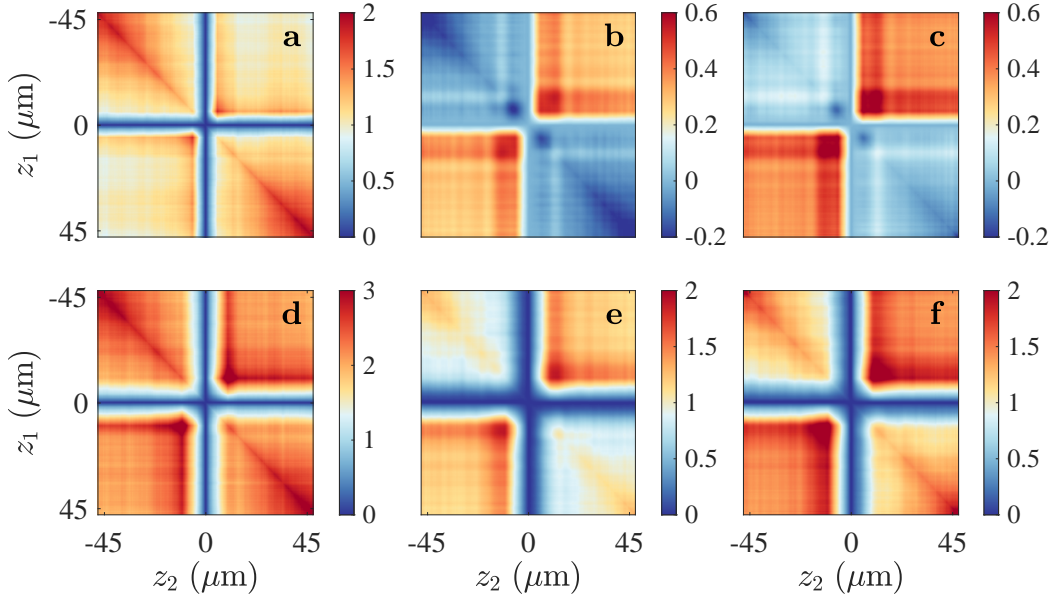
Figure 10: Time of flight (TOF) reconstruction of connected fourth-order correlation function $G_{\mathrm{con}}^{(4)}$ cut at $z_3 = -z_4 = 5.5\ \mu m$ (**a**- **c**) and $z_3 = -z_4 = 10\ \mu m$ (**d-f**). All panels are reconstructed with 2500 realizations of 15 ms TOF with different expansion models. The first column (**a**, **d**) involves only transversal expansion, the second column (**b**, **e**) includes longitudinal expansion but with common phase kept at zero while the third column (**c**, **f**) includes both longitudinal expansion and common phase sampled from a thermal distribution with $T_+ = 75$ nK. The edge data of length 2.5 μm on each end have been omitted to suppress boundary effects.

Figure 11: Time of flight (TOF) reconstruction of disconnected fourth-order correlation function $G_{\mathrm{dis}}^{(4)}$ cut at $z_3 = -z_4 = 5.5\ \mu m$ (**a-c**) and $z_3 = -z_4 = 10\ \mu m$ (**d - f**). Each panel corresponds to the same TOF models and parameter regime as in Fig. 10.

the Gaussian regime of $q = 0.5$, the four-point correlation function indeed factorizes into the products and sum of contributions coming from the two-point function (disconnected part), barring some fluctuations due to finite statistics (see Fig. 22 in Appendix E). Here, we will focus only on the $G^{(4)}$ reconstruction of non-Gaussian states, which contains information about four-body correlation. However, a direct comparison between input and output correlation functions is not straightforward for higher dimensional data. For visualization, we fix a cut at two different lengths $z_3 = -z_4 = 5.5$ μm and $z_3 = -z_4 = 10$ μm. From Fig. 10, we find that in both cases TOF allows a faithful reconstruction of the connected correlator. However, the disconnected part appears to be considerably modified by TOF as shown in Fig. 11. The effect of TOF is especially profound for short distance cut at $z_3 = -z_4 = 5.5$ μm (Figs. 11a-c) where we find correlations which are different from insitu not only quantitatively but also qualitatively. In this regime, the correlation is dominated by systematical deviations generated by longitudinal expansion.

We hypothesize that this systematic is due to the movement of the atoms during longitudinal expansion, i.e. the atoms at z insitu already move a distance of $\sim z \pm \ell_t$ after time of flight which is a physical mechanism behind the systematic phase shift error in Eq. (9). This can also be seen from Fig. 9 where the cut $z_3 = -z_4 = 5.5$ μm is still located in the region dominated by TOF systematics, i.e. the expanding cross region in the middle of Fig. 9. Consequently, it introduces an extra positive correlation in the off-diagonal block and a negative correlation in the diagonal block. When we probe longer distance cut $z_3 = -z_4 = 10$ μm, however, the input and output/reconstructed correlation appear more similar to each other than the shorter cut, but still with a slight asymmetry between the diagonal and off-diagonal blocks, and a discrepancy in the absolute value of the correlation.

Our results highlight the importance of considering measurement systematics from time of flight when looking into higher order correlation data [42]. Although the connected part of the correlation appears conserved by TOF, the disconnected part is affected. This may then distort the overall result, i.e. measure of non-Gaussianity. However, this systematic effect is dominant in short-length scale of ~ 5 μm as compared to the typical cut in experiments of around ~ 15 μm. A shorter cut is usually not taken in experiments due to the blurring of imaging systematics, which will be explained in the next section.

5 The effect of image processing

In the previous section, we discussed how the systematic error generated during longitudinal expansion propagates into the measurement of the physical properties of the gas. We find that TOF reconstruction is robust against the systematic phase shift induced by longitudinal dynamics for observables that mostly rely on low-energy excitations with long wavelengths. On the other hand, for some quantities such as velocity-velocity correlation and mean occupation number, the details of fluctuations with shorter wavelengths might matter and so we observe some qualitative differences between the input and the reconstructed quantity.

To check if our analysis also holds in a realistic experimental setting, it is necessary to include the effects introduced by the experimental implementation of the imaging. These include foremost the finite imaging resolution of the imaging optics, the finite pixel size and the readout noise of the camera. In an ideal setting, the readout noise is given by the photon shot noise of the detected light. Furthermore, it includes physical processes that occur during imaging. For example, as the atomic cloud scatters light, it receives a momentum transfer which can lead to diffusion of the atoms in the imaging plane. Moreover, in absorption imaging, the incoming light is in the imaging direction, which may push the image out of focus. In addition, the cloud is also falling under gravity during the exposure time. All together result
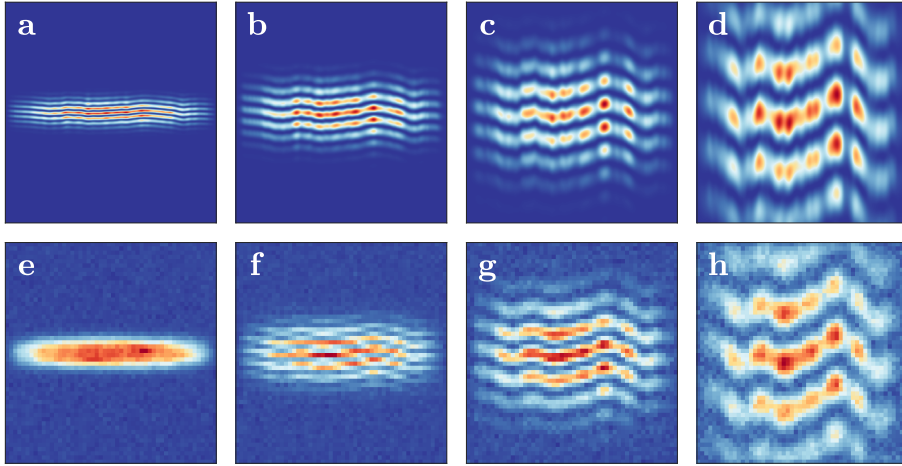
Figure 12: Time of flight density interference image before (**a-d**) and after image processing (**e - h**). The expansion times are 1.5 ms (**a**, **e**), 3.5 ms (**b**, **f**) 7 ms (**c**, **g**), and 15 ms (**d,h**). The input relative and common phase profiles are identical to that of Fig. 2.

in a washing out of short-distance patterns leading to an effective high-frequency cut-off in the imaging function. For a detailed analysis of short wavelength (high momentum) physics, this high-frequency cut-off needs to be determined with exceptional care, mostly from numerical modelling of all the physical effects participating in the specific implementation of the measurement. See Ref. [22] for a more detailed discussion of experimental imaging systematics.

In our numerical study, we take into account these effects by processing our TOF density image as in Refs. [10,22]. Consequently, the code is fine-tuned to the parameters of the specific experiment. For instance, the pixel size is set to be approximately 2 μm, and the defocusing of the camera is set to be 32.7 μm which consists of 25 μm recoil and 7.7 μm due to free-falling during 50 μs exposure time. Prior analysis [22] has shown that the effective result of all the imaging systematics is to induce an exponential momentum cutoff $\sim \exp(-k^2 \sigma_{cutoff}^2)$ where σ_{cutoff} depends on the specifics of the experiments and system parameters. In our simulation, the cutoff is approximately $\sigma_{cutoff} \sim 2.5$ μm.

The comparisons between density images before and after image processing for various expansion times are shown in Fig. 12. For a very short expansion time ($t = 1.5$ ms), the fringe spacing ($\lambda = ht/md \approx 2.3$ μm) is still too small to be resolved by the imaging. By $t = 3.5$ ms ($\lambda \approx 5.4$ μm), the interference fringe is finally resolved and one can start extracting the phase reliably, although with a significantly lower contrast as compared to the unprocessed image (see Fig. 16 in Appendix E). After $t = 3.5$ ms, the qualitative differences between the density image mostly appear in the density ripple as one can see by comparing Fig. 12g and Fig. 12h. Furthermore, after this limit, image processing only modifies the Gaussian width of the cloud and introduces momentum cutoff, thus effectively smoothening short wavelength fluctuations in the extracted fit parameters (see Fig. 13).

To check the robustness of our analytical systematic phase shift formula (9), we perform the same numerical experiment as in Sec. 3 where we encode and decode a smooth single-mode phase profile with TOF simulation but additionally include image processing to the encoding step. The result is shown in Fig. 17 of Appendix E. We find that the dominant correction due to mixing with the common phase is still present even after taking into account imaging systematics. On the contrary, the higher order correction term that arises purely due to the Green's function gets blurred by noise and other experimental imaging systematics. Thus, we
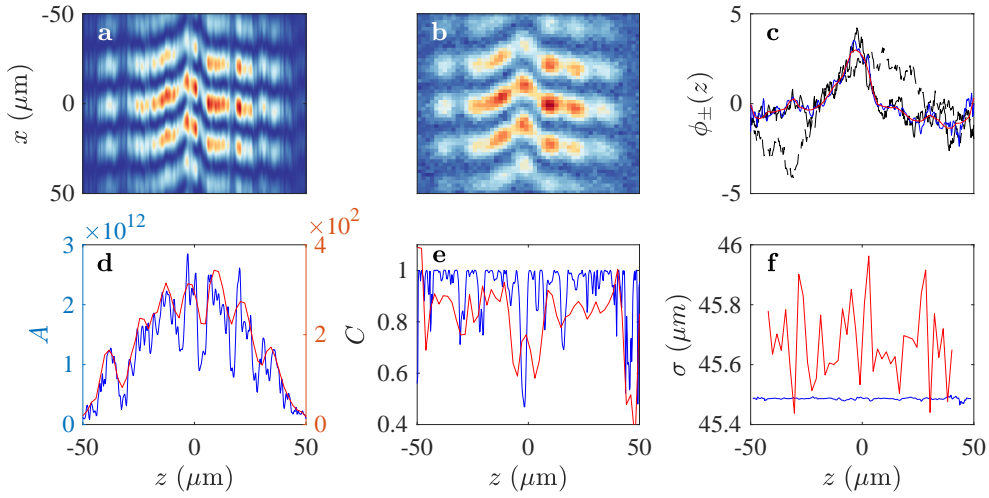
Figure 13: Comparison between single-shot relative phase extraction with and without image processing. Panel **a** (**b**) shows density without (with) image processing after 15 ms time of flight. The extracted relative phase is shown in panel **c** where blue (red) denotes the result extracted from TOF density without (with) image processing. The black solid line is the input relative phase and the dashed black line is the common phase. Panels (**d**-**f**) show the other fit parameters: amplitude $A(z)$, contrast $C(z)$, and width $\sigma_t(z)$ with the blue (red) color denoting the fit parameters extracted from TOF without (with) image processing. This figure demonstrates that image processing only modifies the Gaussian width of the cloud and smoothens short wavelength fluctuations in the extracted fit parameters.

expect that some features of the physical quantities that arise in the high momentum mode due to Green's function dynamics will also get blurred after image processing. This is indeed what we observed in the numerical simulation for the reconstruction of physical quantities associated with Gaussian Luttinger liquid theories. For quantities that rely on long wavelength fluctuation such as two-point phase correlation function (4.1) and full distribution function (4.2), TOF reconstruction is insensitive to image processing (see Figs. 18-19 in Appendix E). On the other hand, the qualitative effects we observe in the TOF reconstruction of Fourier modes and velocity-velocity correlation due to the dynamics of high mode get washed out after taking into account image processing (see Figs. 20 -21 in Appendix E). Lastly, for the fourth-order correlation in the non-Gaussian regime, we find that the slight asymmetry between the diagonal and off-diagonal plateaus of the cut disconnected correlation is still present, although much weaker than without image processing (see Fig. 14).

6 Summary & Discussion

In summary, we derived an analytical expression for systematic phase shift error due to longitudinal expansion, specifically due to mixing with the common degrees of freedom and the presence of longitudinal Green's function. We also assessed the error propagation in the reconstruction of physical quantities related to the statistics of the relative phase field. We find that Gaussian observables and two-point correlations are well-preserved by the TOF measurement since those depend mostly on low momentum phase fluctuation. However, for higher moments and observables sensitive to high momentum fluctuation, we observe that TOF introduces some deviations so they must be taken with great care.
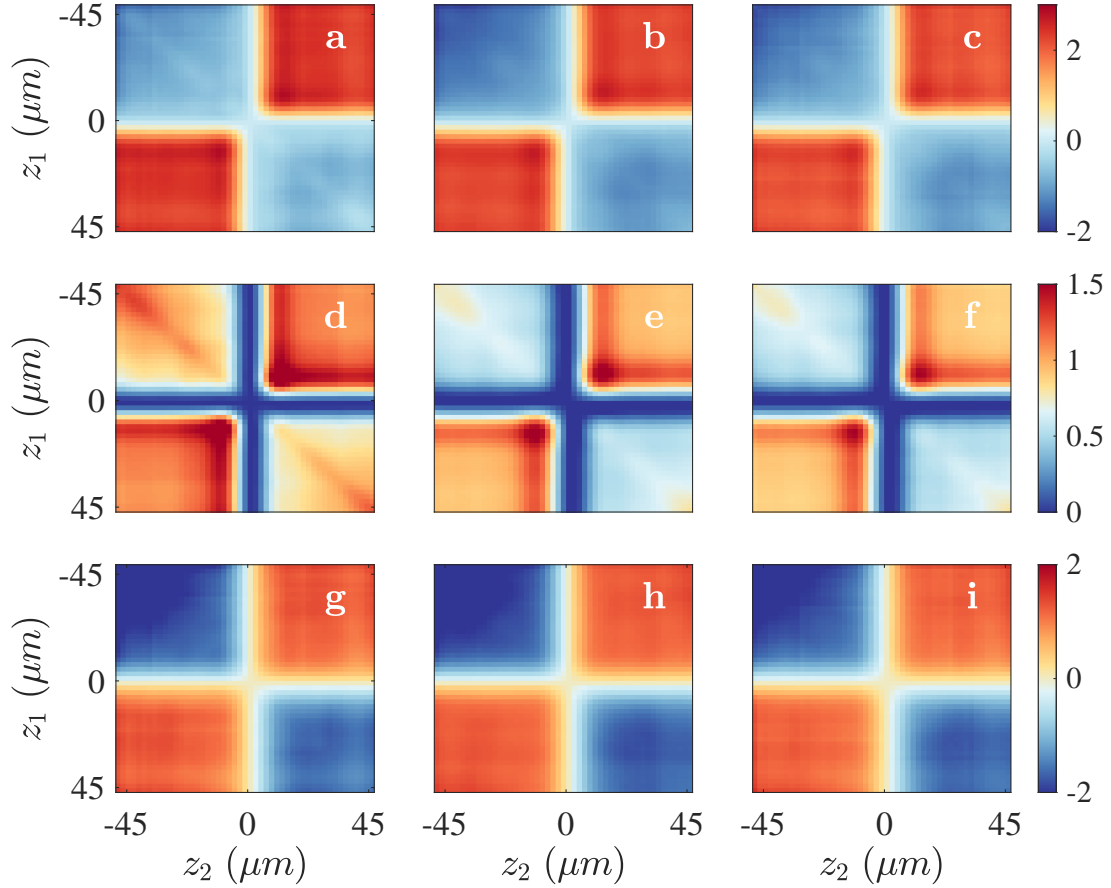
Figure 14: Time of flight (TOF) reconstruction of fourth-order correlation function $G^{(4)}(z_1, z_2, z_3, z_4)$ of the sine-Gordon model in the non-Gaussian regime ($q = \lambda_T/l_J = 3$) taking into account image processing. The data is cut at $z_3 = -z_4 = 11.5\,\mu$m for visualization. Panels (**a-c**) show the full correlation, panels (**d** - **f**) show the disconnected part, and panels (**g** - **i**) shows the connected part. The first column (**a, d, g**) represents the case with only transversal expansion and imaging, the second column (**b, e, h**) includes longitudinal expansion and imaging but with common phase kept at zero and the last column (**c, f, i**) corresponds to the case with longitudinal expansion, image processing, and common phase sampled from thermal distribution with $T_+ = 75$ nK. Each panel is reconstructed from 2500 TOF realizations with 15 ms expansion time. The edge data of length 2.5 μm on each end have been omitted to suppress boundary effects.

For these quantities, one can then think about correcting the systematic deviation or improving the measurement. To improve on the readout of these 1D quantum simulators one can implement atom optical elements during the time of flight. Implementing a weak cylindrical lens (harmonic potential along the longitudinal direction applied for a finite time) projects the image to infinity and will result in transforming the time of flight measurement into a measurement of longitudinal momentum [43]. Implementing a stronger cylindrical lens leads to direct imaging of the longitudinal in-situ coordinate into the imaging plane [44]. The latter will also allow us to enlarge the image and gain considerable improvement in longitudinal imaging resolution, and it will solve problems caused by the longitudinal expansion and mixing between common and relative degrees of freedom caused by the finite temperature of the trapped quantum gas. Both options will be explored in detail in future work.

The analysis done in this paper is subjected to the validity of the modelling approximations [see Fig. 1]. One approximation we made was to ignore the broadening due to atomic repulsion $\sigma_0^2(z) = \sigma_0^2\sqrt{1 + 2a_s n_0(z)} \approx \sigma_0^2$. Relaxing this assumption makes it difficult to obtain an analytical relation between the initial state and the final measured density due to the non-separability of the initial state. However, assuming that the non-separability is weak, there exists an ansatz [22] that can phenomenologically capture the most relevant features of interference image broadened by scattering. The ansatz is to replace all σ_0 appearing in Eq. (4) by the broadened $\sigma_0(z)$. Note that the fringe spacing now also depends on z, i.e. $k(z,t) = d/(\sigma_0^2(z)\omega_\perp t)$. Taking longitudinal expansion into account, we can develop a similar ansatz to modify Eq. (5). We replace all σ_0 with $\sigma_0(z')$ and propagate it with a Green's function. Preliminary numerical simulation with this ansatz has revealed that scattering only affects the width of the final image, but it does not significantly affect other extracted fit parameters [Fig. 15 in Appendix E].

Furthermore, throughout this paper, we have ignored the impact of density fluctuations by assuming $\delta n_{1,2} \ll n_0$ which might not be accurate in higher temperatures. We will address the effect of density fluctuation in future work. Moreover, we have assumed that the time of flight expansion is fully ballistic. A more refined modelling would be to include the hydrodynamic effect at the initial phase of the expansion, where interaction energy still remains in the system. Only after interaction energy sufficiently decays, does the system follow fully ballistic dynamics. A further direction of work will be to include the final state interaction during the initial expansion. This will be important when studying systems in the 1D-3D cross-over when the fast switch-off of interactions can no longer be guaranteed.

In addition to refining the model, another future direction is to extract the common phase from TOF interference pattern. From this study, we find that information about the common phase is imprinted on the density ripple. Density ripple has been used for thermometry in the case of single condensate [10, 20]. However, the significance of density ripple in the two condensates case has not been explored. Developing a readout method of the common phase from density ripple could be useful in unlocking the full potential of 1D Bose gas interference experiments, especially in non-equilibrium. For example, it is known that the higher order correction to the sine-Gordon model for describing tunnel-coupled 1D Bose gas involves a coupling between relative and common phase [24, 33]. Moreover, density imbalances between atoms in the two double wells can also lead to coupling between relative and common phases, leading to double-light cone thermalization [29]. Finally, having access to a common phase could also allow us to simulate spin-charge transport in 1D Bose gases [29, 40]. This work serves as a fundamental starting point for further research in this direction.

In conclusion, our study underscores two significant findings. Firstly, it provides a comprehensive understanding of various systematics sources in local relative phase reconstruction with time of flight measurement. Secondly, it identifies avenues and regimes for enhancing modelling methods to achieve more accurate reconstructions. In addition, we also observe the

potential for extracting additional information from TOF measurements [45], thus augmenting the measurement capabilities of cold atomic quantum simulators. These advancements may serve to enhance future explorations of the physics of cold atomic systems.

7 Acknowledgments

References

[1] A. D. Cronin, J. Schmiedmayer and D. E. Pritchard, *Optics and interferometry with atoms and molecules*, Rev. Mod. Phys. **81**(3), 1051 (2009).

[2] T. Langen, R. Geiger and J. Schmiedmayer, *Ultracold atoms out of equilibrium*, Annu. Rev. Cond. Mat. Phys. **6**, 201 (2015).

[3] S. Hofferberth, I. Lesanovsky, B. Fischer, T. Schumm and J. Schmiedmayer, *Non-equilibrium coherence dynamics in one-dimensional bose gases*, Nature **449**, 324 (2007).

[4] T. Langen, R. Geiger, M. Kuhnert, B. Rauer and J. Schmiedmayer, *Local emergence of thermal correlations in an isolated quantum many-body system*, Nature Phys. **9**, 640 (2013), doi:10.1038/nphys2739.

[5] T. Langen, S. Erne, R. Geiger, B. Rauer, T. Schweigler, M. Kuhnert, W. Rohringer, I. E. Mazets, T. Gasenzer and J. Schmiedmayer, *Experimental observation of a generalized Gibbs ensemble*, Science **348**, 207 (2015), doi:10.1126/science.1257026.

[6] M. Tajik, I. Kukuljan, S. Sotiriadis, B. Rauer, T. Schweigler, F. Cataldini, J. Sabino, F. Møller, P. Schüttelkopf, S.-C. Ji *et al.*, *Verification of the area law of mutual information in a quantum field simulator*, Nature Physics pp. 1–5 (2023).

[7] M. Gluza, J. Sabino, N. H. Ng, G. Vitagliano, M. Pezzutto, Y. Omar, I. Mazets, M. Huber, J. Schmiedmayer and J. Eisert, *Quantum field thermal machines*, PRX Quantum **2**(3), 030310 (2021).

[8] J. Schmiedmayer, *One-dimensional atomic superfluids as a model system for quantum thermodynamics*, In *Thermodynamics in the Quantum Regime: Fundamental Aspects and New Directions*, pp. 823–851. Springer (2019).

[9] A. Imambekov, V. Gritsev and E. Demler, *Ultracold Fermi gases, Proc. Internat. School Phys. Enrico Fermi, 2006*, chap. Fundamental noise in matter interferometers, IOS Press, Amsterdam, The Netherlands (2007).

[10] F. Møller, T. Schweigler, M. Tajik, J. a. Sabino, F. Cataldini, S.-C. Ji and J. Schmiedmayer, *Thermometry of one-dimensional bose gases with neural networks*, Phys. Rev. A **104**, 043305 (2021), doi:10.1103/PhysRevA.104.043305.

[11] M. Pigneur, T. Berrada, M. Bonneau, T. Schumm, E. Demler and J. Schmiedmayer, *Relaxation to a phase-locked equilibrium state in a one-dimensional bosonic josephson junction*, Phys. Rev. Lett. **120** (2018), doi:10.1103/physrevlett.120.173601.

[12] M. Gluza, T. Schweigler, M. Tajik, J. Sabino, F. Cataldini, F. S. Møller, S.-C. Ji, B. Rauer, J. Schmiedmayer, J. Eisert and S. Sotiriadis, *Mechanisms for the emergence of Gaussian correlations*, SciPost Phys. **12**, 113 (2022), doi:10.21468/SciPostPhys.12.3.113.

[13] S. Hofferberth, I. Lesanovsky, T. Schumm, A. Imambekov, V. Gritsev, E. Demler and J. Schmiedmayer, *Probing quantum and thermal noise in an interacting many-body system*, Nature Physics **4**(6), 489 (2008).

[14] T. Kitagawa, A. Imambekov, J. Schmiedmayer and E. Demler, *The dynamics and prethermalization of one-dimensional quantum systems probed through the full distributions of quantum noise*, New J. Phys. **13**(7), 073018 (2011), doi:10.1088/1367-2630/13/7/073018.

[15] M. Gluza, T. Schweigler, B. Rauer, C. Krumnow, J. Schmiedmayer and J. Eisert, *Quantum read-out for cold atomic quantum simulators*, Comm. Phys. **3**, 12 (2020), doi:10.1038/s42005-019-0273-y.

[16] T. Schweigler, V. Kasper, S. Erne, I. Mazets, B. Rauer, F. Cataldini, T. Langen, T. Gasenzer, J. Berges and J. Schmiedmayer, *Experimental characterization of a quantum many-body system via higher-order correlations*, Nature **545**, 323 (2017).

[17] T. V. Zache, T. Schweigler, S. Erne, J. Schmiedmayer and J. Berges, *Extracting the field theory description of a quantum many-body system from experimental data*, Phys. Rev. X **10**, 011020 (2020), doi:10.1103/PhysRevX.10.011020.

[18] T. Langen, R. Geiger, M. Kuhnert, B. Rauer and J. Schmiedmayer, *Local emergence of thermal correlations in an isolated quantum many-body system*, Nature Phys. **9**, 640 (2013).

[19] M. Tajik, M. Gluza, N. Sebe, P. Schüttelkopf, F. Cataldini, J. Sabino, F. Møller, S.-C. Ji, S. Erne, G. Guarnieri *et al.*, *Experimental observation of curved light-cones in a quantum field simulator*, Proceedings of the National Academy of Sciences **120**(21), e2301287120 (2023).

[20] A. Imambekov, I. E. Mazets, D. S. Petrov, V. Gritsev, S. Manz, S. Hofferberth, T. Schumm, E. Demler and J. Schmiedmayer, *Density ripples in expanding low-dimensional gases as a probe of correlations*, Phys. Rev. A **80**, 033604 (2009), doi:10.1103/PhysRevA.80.033604.

[21] Y. D. van Nieuwkerk, J. Schmiedmayer and F. Essler, *Projective phase measurements in one-dimensional Bose gases*, SciPost Physics **5**, 046 (2018), doi:10.21468/scipostphys.5.5.046.

[22] T. Schweigler, *Correlations and dynamics of tunnel-coupled one-dimensional Bose gases*, Ph.D. thesis, TU Wien, arxiv:1908.00422 (2019).

[23] T. Langen, *Non-equilibrium dynamics of one-dimensional Bose gases*, Springer (2015).

[24] Y. D. van Nieuwkerk, J. Schmiedmayer and F. H. Essler, *Josephson oscillations in split one-dimensional bose gases*, arXiv preprint arXiv:2010.11214 (2020).

[25] J.-F. Mennemann, S. Erne, I. Mazets and N. J. Mauser, *The discrete green's function method for wave packet expansion via the free schrödinger equation*, arXiv preprint arXiv:2303.09464 (2023).

[26] D. A. Smith, M. Gring, T. Langen, M. Kuhnert, B. Rauer, R. Geiger, T. Kitagawa, I. Mazets, E. Demler and J. Schmiedmayer, *Prethermalization revealed by the relaxation dynamics of full distribution functions*, New Journal of Physics **15**(7), 075011 (2013).

[27] M. Rigol, V. Dunjko, V. Yurovsky and M. Olshanii, *Relaxation in a completely integrable many-body quantum system: An ab initio study of the dynamics of the highly excited states of 1D lattice hard-core bosons*, Phys. Rev. Lett. **98**, 050405 (2007), doi:10.1103/PhysRevLett.98.050405.

[28] L. Salasnich, A. Parola and L. Reatto, *Transition from three dimensions to one dimension in bose gases at zero temperature*, Phys. Rev. A **70**, 013606 (2004), doi:10.1103/PhysRevA.70.013606.

[29] T. Langen, T. Schweigler, E. Demler and J. Schmiedmayer, *Double light-cone dynamics establish thermal states in integrable 1d bose gases*, New Journal of Physics **20**(2), 023034 (2018).

[30] C. M. Bender and S. A. Orszag, *Advanced mathematical methods for scientists and engineers I: Asymptotic methods and perturbation theory*, Springer Science & Business Media (2013).

[31] C. Mora and Y. Castin, *Extension of Bogoliubov theory to quasicondensates*, Phys. Rev. A **67**, 053615 (2003), doi:10.1103/PhysRevA.67.053615.

[32] T. Schweigler, V. Kasper, S. Erne, I. E. Mazets, B. Rauer, F. Cataldini, T. Langen, T. Gasenzer, J. Berges and J. Schmiedmayer, *Experimental characterization of a quantum many-body system via higher-order correlations*, Nature **545**(7654), 323 (2017), doi:10.1038/nature22310.

[33] V. Gritsev, A. Polkovnikov and E. Demler, *Linear response theory for a pair of coupled one-dimensional condensates of interacting atoms*, Phys. Rev. B **75**, 174511 (2007), doi:10.1103/PhysRevB.75.174511.

[34] T. Murtadho, M. Gluza and A. Z. Khatee, *ToF_expansion*, https://github.com/inQ-NTU/ToF_expansion.

[35] S. Beck, I. E. Mazets and T. Schweigler, *Nonperturbative method to compute thermal correlations in one-dimensional systems*, Phys. Rev. A **98**, 023613 (2018), doi:10.1103/PhysRevA.98.023613.

[36] C. W. Gardiner *et al.*, *Handbook of stochastic methods*, vol. 3, springer Berlin (1985).

[37] T. Giamarchi, *Quantum Physics in One Dimension*, Oxford University Press, Oxford, doi:10.1093/acprof:oso/9780198525004.001.0001 (2003).

[38] B. Rauer, S. Erne, T. Schweigler, F. Cataldini, M. Tajik and J. Schmiedmayer, *Recurrences in an isolated quantum many-body system*, Science **359**(360), 307 (2018), doi:10.1126/science.aan7938.

[39] M. Gring, M. Kuhnert, T. Langen, T. Kitagawa, B. Rauer, M. Schreitl, I. E. Mazets, D. A. Smith, E. Demler and J. Schmiedmayer, *Relaxation and prethermalization in an isolated quantum system*, Science **337**, 1318 (2012).

[40] T. Kitagawa, A. Imambekov, J. Schmiedmayer and E. Demler, *The dynamics and prethermalization of one-dimensional quantum systems probed through the full distributions of quantum noise*, New J. Phys. **13**(7), 073018 (2011).

[41] H.-P. Stimming, N. J. Mauser, J. Schmiedmayer and I. Mazets, *Fluctuations and stochastic processes in one-dimensional many-body quantum systems*, Phys. Rev. Lett. **105**(1), 015301 (2010), doi:10.1103/PhysRevLett.105.015301.

[42] T. Schweigler, V. Kasper, S. Erne, I. Mazets, B. Rauer, F. Cataldini, T. Langen, T. Gasenzer, J. Berges and J. Schmiedmayer, *Experimental characterization of a quantum many-body system via higher-order correlations*, Nature **545**, 323 (2017), doi:10.1038/nature22310.

[43] I. Shvarchuck, C. Buggle, D. S. Petrov, K. Dieckmann, M. Zielonkowski, M. Kemmann, T. G. Tiecke, W. von Klitzing, G. V. Shlyapnikov and J. T. M. Walraven, *Bose-einstein condensation into nonequilibrium states studied by condensate focusing*, Phys. Rev. Lett. **89**, 270404 (2002), doi:10.1103/PhysRevLett.89.270404.

[44] L. Asteria, H. P. Zahn, M. N. Kosch, K. Sengstock and C. Weitenberg, *Quantum gas magnifier for sub-lattice-resolved imaging of 3d quantum systems*, Nature **599**(7886), 571 (2021).

[45] T. Murtadho, F. Cataldini, S. Erne, M. Gluza, J. Schmiedmayer and N. H. Ng, *Measurement of total phase fluctuation in cold-atomic quantum simulator*, arXiv:2408.03736 (2024), doi:https://arxiv.org/abs/2408.03736.

A   Free expansion dynamics

In this Appendix, we will derive the expansion dynamics of the Bosonic fields including both transversal and longitudinal dynamics, elucidating earlier works by Yuri, Essler, and Schmiedmayer [21]. Let us consider the 3D time-dependent Gross-Pitaevskii equation

$$i\hbar\frac{\partial \Psi}{\partial t} = -\frac{\hbar^2}{2m}\nabla^2\Psi + V(x,y,z)\Psi + g|\Psi|^2\Psi. \tag{18}$$

Upon free expansion, we set all trapping potential to zero $V(x,y,z) = 0$ and we neglect final state interaction $g = 0$, so that the equation of motion is essentially that of free particles.

Then, the time evolution is given by convolution with a Green's function

$$\Psi(\vec{r},z,t) = \int d^2\vec{r}' \, dz \, G(\vec{r}-\vec{r}',t)G(z-z',t)\Psi(\vec{r}',z,0), \tag{19}$$

where we have separated the transversal $\vec{r} = (x,y)$ and longitudinal z components of the evolution and that $G(\xi,t) = \sqrt{m/2\pi i\hbar t}\exp(-m\xi^2/2i\hbar t)$ is the free, single-particle Green's function. Next, we substitute the initial state [Eq. (1) in the main text] and integrate over the transverse directions, giving us the time-evolved fields

$$\Psi_{1,2}(x,y,z,t) = \frac{1}{\sqrt{\pi\sigma_0^2(1+i\omega_\perp t)^2}}\exp\left(-\frac{(x\pm d/2)^2+y^2}{2\sigma_0^2(1+i\omega_\perp t)}\right)\exp\left(\frac{im[(x\pm d/2)^2+y^2]}{2\hbar t}\right)$$

$$\times \int dz' \, G(z-z',t)\sqrt{n_0(z')}e^{i\phi_{1,2}(z')}. \tag{20}$$

where we have assumed $\omega_\perp t \gg 1$ and explicitly ignored density fluctuation $\delta n_{1,2} \ll n_0$.

We are concerned with the density after coherent superposition of the two fields as they overlap, integrated along the vertical direction (y-axis), i.e.

$$\rho_{\text{TOF}}(x,z,t) = \int dy \, |\Psi_1(\vec{r},z,t) + \Psi_2(\vec{r},z,t)|^2. \tag{21}$$

By substituting Eq. (20) to Eq. (21), we will obtain a transverse Gaussian envelope of width $\sigma_\tau = \sigma_0 \sqrt{1 + \omega_\perp^2 t^2}$. If we wait long enough such that $d \ll \sigma_t$ the transverse Gaussian envelopes can be approximated into a single Gaussian centred at the origin. Consequently, the expression for ρ_{TOF} becomes relatively simple

$$\rho_{\text{TOF}}(x,z,t) = A e^{-\frac{x^2}{\sigma_t^2}} \left| \int_{-L/2}^{L/2} dz' \, G(z-z',t) \sqrt{n_0(z')} e^{i\phi_+(z')/2} \cos\left(\frac{kx + \phi_-(z')}{2}\right) \right|^2. \tag{22}$$

with A being a normalization constant, $k = md/(\hbar t)$ is the inverse fringe spacing, $\phi_\mp(z) = \phi_2(z) \mp \phi_1(z)$ are relative (-) and common (+) phases.

B Derivation of the transverse fit formula

We continue to derive the transversal fit formula [Eq. (4) in the main text] including the effects of mean density imbalance as well as density fluctuations. This section is a restatement of other similar derivations in the literature [21–23].

We start from the extended version of Eq. (4) in the main text, taking into account density fluctuations and different mean densities in each well

$$\rho_{\text{TOF}}(x,z,t) = A e^{-x^2/\sigma_t^2} \left| \int_{-L/2}^{L/2} dz' G(z'-z,t) e^{i\phi_+(z')/2} \left[\sqrt{n_1(z') + \delta n_1(z')} e^{-i\phi_-(z')/2} e^{-ikx/2} \right. \right.$$
$$\left. \left. + \sqrt{n_2(z') + \delta n_2(z')} e^{i\phi_-(z')/2} e^{ikx/2} \right] \right|^2. \tag{23}$$

Next, we ignore longitudinal dynamics by substituting $G(z-z',t) \to \delta(z-z')$ and integrate over z'

$$\rho_{\text{TOF}}^\perp(x,z,t) = A e^{-x^2/\sigma_t^2} \left| \sqrt{n_1(z) + \delta n_1(z)} e^{-i\frac{kx+\phi_-(z)}{2}} + \sqrt{n_2(z) + \delta n_2(z)} e^{i\frac{kx+\phi_-(z)}{2}} \right|^2$$
$$\cong A e^{-x^2/\sigma_t^2} [n_+(z) + \delta n_+(z)][1 + C(z)\cos(kx + \phi_-(z)], \tag{24}$$

where

$$n_+(z) = n_1(z) + n_2(z) \qquad \delta n_+(z) = \delta n_1(z) + \delta n_2(z), \tag{25}$$

and interference contrast $C(z)$

$$C(z) = \frac{2\sqrt{(n_1(z) + \delta n_1(z))(n_2(z) + \delta n_2(z))}}{n_+(z) + \delta n_+(z)}. \tag{26}$$

Note that contrast is maximum $C(z) = 1$ when $n_1(z) = n_2(z)$ and $\delta n_1(z) = \delta n_2(z) = 0$. After absorbing $n_+(z), \delta n_+(z)$ into the normalization constant A, we recover Eq. (4) in the main text.

C Corrections due to longitudinal dynamics

Here, we present a detailed derivation of the new analytical results contained in the main text [Eqs. (7) - (9)]. We start from the full expansion formula [Eq. (5) in the main text]

$$\rho_{\text{TOF}}(x,z,t) = A(t)e^{-x^2/\sigma_t^2} \left| \int_{-L/2}^{L/2} dz' G(z-z',t)I(x,z',t) \right|^2, \qquad (27)$$

where

$$I(x,z',t) = \sqrt{n_0(z')}e^{i\phi_+(z')/2} \cos\left(\frac{kx + \phi_-(z')}{2} \right). \qquad (28)$$

We treat longitudinal expansion perturbatively by performing Taylor expansion of $I(x,z',t)$ around small $\Delta z = z' - z$

$$I(x,z',t) = I(x,z,t) + \Delta z\, \partial_z I + \frac{\Delta z^2}{2}\partial_z^2 I + O(\Delta z^3). \qquad (29)$$

Substituting Eq. (29) to the integral in Eq. (27), we find that the zeroth order term will give us the transversal expansion formula with a maximum contrast $C = 1$

$$\rho_{\text{TOF}}^{\perp}(x,z,t) \approx A(t)e^{-x^2/\sigma_t^2}\left| I(x,z,t) \int_{-\infty}^{\infty} G(\Delta z,t)\, d(\Delta z) \right|^2$$

$$= \frac{A(t)n_0(z)}{2}e^{-x^2/\sigma_t^2}[1 + \cos(kx + \phi_-(z))], \qquad (30)$$

where we have extended the integration limit from $[-L/2, L/2]$ to $(-\infty, \infty)$.

Let us now compute the higher-order corrections. The first order term will vanish because it is proportional to $\int_{-\infty}^{\infty}(\Delta z\, G(\Delta z,t))\, d(\Delta z) = 0$. Therefore, the next non-zero correction will come from the second-order term,

$$\rho_{\text{TOF}}(x,z,t) \approx A(t)e^{-x^2/\sigma_t^2}\left| I + \frac{\partial_z^2 I}{2}\int_{-\infty}^{\infty}(\Delta z^2 G(\Delta z,t))\, d(\Delta z) \right|^2. \qquad (31)$$

It is easy to check that $\int_{-\infty}^{\infty}(\Delta z^2 G(\Delta z,t))d(\Delta z) = \frac{i\hbar t}{m} = i\ell_t^2$ where we have defined $\ell_t = \sqrt{\hbar t/m}$ to be the length scale of longitudinal expansion. Substituting the integral and defining a derivative with respect to scaled coordinate $\eta = z/\ell_t$, one obtains

$$\rho_{\text{TOF}}(x,z,t) \approx A(t)e^{-x^2/\sigma_t^2}\left| I + \frac{1}{2}i\, \partial_\eta^2 I \right|^2 \qquad (32)$$

$$= \rho_{\text{TOF}}^{\perp}(x,z,t) + A(t)e^{-x^2/\sigma_t^2}\left[-\text{Im}(I^*\partial_\eta^2 I) + \frac{1}{4}|\partial_\eta^2 I|^2 \right] \qquad (33)$$

$$= \rho_{\text{TOF}}^{\perp}(x,z,t) + \Delta\rho^{(2)} + \Delta\rho^{(4)} \qquad (34)$$

with $\Delta\rho^{(n)}$ being the n-th order correction terms in scaled derivatives $\partial_\eta I$ which we expect to be small [see the main text for reasoning].

We first focus on the leading order correction $\Delta\rho^{(2)} = -A(t)e^{-x^2/\sigma_t^2}\text{Im}(I^*\partial_\eta^2 I)$. To compute this term, we must first compute $\partial_z^2 I = \ell_t^{-2}\partial_\eta^2 I$

$$\partial_z^2 I = \Gamma(z)\cos\left(\frac{kx + \phi_-(z)}{2} \right) - \Lambda(z)\sin\left(\frac{kx + \phi_-(z)}{2} \right), \qquad (35)$$

where

$$\Gamma(z) = \partial_z^2 \psi_+ - \frac{\psi_+(\partial_z\phi_-)^2}{4} \qquad \Lambda(z) = \partial_z\psi_+\partial_z\phi_- + \frac{\psi_+\partial_z^2\phi_-}{2} \qquad (36)$$

26

and $\psi_+(z) = \sqrt{n_0(z)}e^{i\phi_+(z)/2}$. For simplicity, we will consider the case $n_0(z) = n_{1D} = \text{const.}$ which gives us

$$\Delta\rho^{(2)} = -A(t)e^{-x^2/\sigma_t^2}\frac{n_0}{4}[\partial_\eta^2\phi_+(1+\cos(kx+\phi_-)) - \partial_\eta\phi_-\partial_\eta\phi_+\sin(kx+\phi_-)]. \tag{37}$$

Combining the above with the expression for $\rho_{\text{TOF}}^{\perp}$ in Eq. (30) and using trigonometric identity $a\cos x + b\sin x = \sqrt{a^2+b^2}\cos(x-\alpha)$ with $\tan\alpha = b/a$ we can express ρ_{TOF} as

$$\rho_{\text{TOF}}(x,z,t) \approx A'(z,t)e^{-x^2/\sigma_t^2}[1 + C(z,t)\cos(kx+\phi_-(z)-\Delta\phi_-^{(2)}(z,t))] \tag{38}$$

with

$$A'(z,t) = \frac{A(t)n_0(z)}{2}\left(1 - \frac{1}{2}\partial_\eta^2\phi_+\right) \tag{39}$$

$$C(z,t) = \frac{1}{\left(1-\frac{1}{2}\partial_\eta^2\phi_+\right)}\sqrt{\left(1-\frac{1}{2}\partial_\eta^2\phi_+\right)^2 + \left(\frac{1}{2}\partial_\eta\phi_-\partial_\eta\phi_+\right)^2} \tag{40}$$

$$\Delta\phi_-^{(2)}(z,t) = \arctan\left(\frac{\frac{1}{2}\partial_\eta\phi_+\partial_\eta\phi_-}{1-\frac{1}{2}\partial_\eta^2\phi_+}\right) \approx \frac{1}{2}\partial_\eta\phi_+\partial_\eta\phi_-. \tag{41}$$

In the main text, we are also interested in cases where $\phi_+ = 0$. For such cases, the above derivation implies $\Delta\phi_-^{(2)} = 0$ and so higher order terms need to be taken into account.

Let us now consider the $\Delta\rho^{(4)}$ term in Eq. (32). Below, we explicitly write the form of $|\partial_z^2 I|^2$,

$$|\partial_z^2 I|^2 = \frac{1}{2}\left(|\Gamma(z)|^2 + |\Lambda(z)|^2\right) + \frac{1}{2}\left(|\Gamma(z)|^2 - |\Lambda(z)|^2\right)\cos(kx+\phi_-(z))$$
$$- \text{Re}\left(\Gamma^*(z)\Lambda(z)\right)\sin(kx+\phi_-(z)). \tag{42}$$

To simplify the expressions, we again use the assumption $n_0 = n_{1D} = \text{const.}$, such that

$$\Gamma(z) = \frac{\sqrt{n_{1D}}}{2\ell_t^2}e^{i\phi_+(z)/2}F(\eta) \qquad \Lambda(z) = \frac{\sqrt{n_{1D}}}{2\ell_t^2}e^{i\phi_+(z)/2}G(\eta), \tag{43}$$

where $F(\eta)$, $G(\eta)$ are dimensionless functions

$$F(\eta) = \partial_\eta^2\phi_+ - \frac{(\partial_\eta\phi_+)^2 + (\partial_\eta\phi_-)^2}{2} \qquad G(\eta) = i(\partial_\eta\phi_+)(\partial_\eta\phi_-) + \partial_\eta^2\phi_-. \tag{44}$$

Thus, the density correction is given by,

$$\Delta\rho^{(4)} = \frac{1}{16}A(t)e^{-x^2/\sigma_t^2}(|F|^2+|G|^2)\left[1 + \frac{|F|^2-|G|^2}{|F|^2+|G|^2}\cos(kx+\phi_-) - \frac{2\text{Re}(F^*G)}{|F|^2+|G|^2}\sin(kx+\phi_-)\right]. \tag{45}$$

Putting $\rho_{\text{TOF}}^{\perp}$, $\Delta\rho^{(2)}$, and $\Delta\rho^{(4)}$ together, one can always recast the entire expression into the form

$$\rho_{\text{TOF}}(x,z,t) \approx A(z,t)e^{-x^2/\sigma_t^2}\left[1 + C(z,t)\cos\left(kx+\phi_-(z)-\Delta\phi_-(z)\right)\right], \tag{46}$$

which is one of the main analytical results of the main text [Eq. (7)]. Note that the validity of Eq. (46) does not depend on the specific forms of $A(z,t)$ and $C(z,t)$. It only relies on the fact that the correction terms are always proportional to $\sin(kx+\phi_-)$ or $\cos(kx+\phi_-)$ and so it will also be valid in varying mean density cases.

In the simplest case of $n_0(z) = n_{1D}$ and $\phi_+(z) = 0$, we find a higher order phase shift

$$\Delta\phi_-^{(4)}(z,t)\Big|_{\phi_+=0} = -\arctan\left(\frac{2\text{Re}(F^*G)}{8 + (|F|^2-|G|^2)}\right) \approx \frac{1}{8}\left(\partial_\eta\phi_-\right)^2\left(\partial_\eta^2\phi_-\right). \tag{47}$$

Summing Eq. (41) with Eq. (47) gives another analytical result of the main text [Eq. (9)].

D Relative phase fitting initialization

In this section, we show the approximate linear relationship between relative phase ϕ_- and the interference peak's transversal position $x_{\max}$ for a fixed longitudinal position z. We use this approximate linear relationship to provide an initial guess for the optimizer used in fitting.

For simplicity, we assume ρ_{TOF} to be well approximated by the standard fitting formula [Eq. (4) in the main text] with $C = 1$. To find the transversal peak location, we simply solve $\partial \rho_{\text{TOF}}^{\perp}/\partial x|_{x=x_{\max}} = 0$, which gives the condition

$$\frac{2x}{\sigma_t^2}\left[1 + \cos\left(kx_{\max} + \phi_-^{(0)}\right)\right] + k\sin\left(kx_{\max} + \phi_-^{(0)}\right) = 0, \tag{48}$$

where the superscript 0 indicates a 'guess' value (initial value to feed into the optimizer). Using the half-angle formula, we obtain

$$\cos\left(\frac{kx_{\max} + \phi_-^{(0)}}{2}\right)\left[\frac{2x}{\sigma_t^2}\cos\left(\frac{kx_{\max} + \phi_-^{(0)}}{2}\right) + k\sin\left(\frac{kx_{\max} + \phi_-^{(0)}}{2}\right)\right] = 0, \tag{49}$$

For non-zero interference, we must have $\cos([kx + \phi_-^{(0)}]/2) \neq 0$ and so to satisfy Eq. (49), the terms inside the parenthesis have to vanish. Finally, we can solve for $\phi_-^{(0)}$ and the result is

$$\phi_-^{(g)} = -kx_{\max} + 2\arctan\left(-\frac{2\omega_\perp t}{1 + \omega_\perp^2 t^2}\frac{x_{\max}}{d}\right) \approx -\frac{md}{\hbar t}x_{\max} \tag{50}$$

where in the last approximation we have used $\omega_\perp t \gg 1$ such that the arctan function changes very slowly with $x_{\max}$.
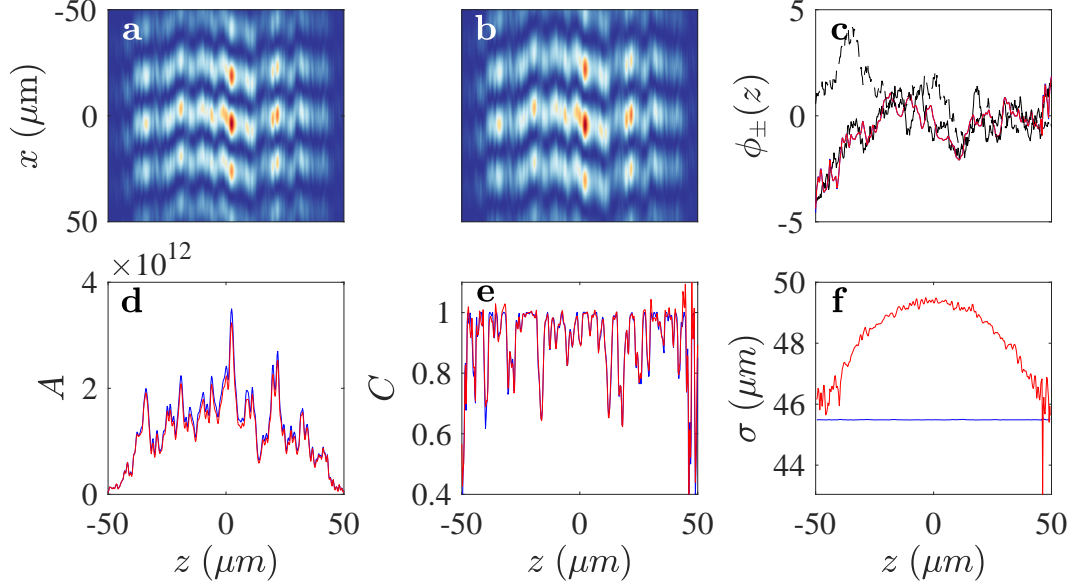
E   Supplementary plots

Figure 15: Single shot relative phase extraction with and without broadening due to atomic repulsion. Panels **a** - **b** show interference pattern without ($\sigma_0 = $ const.) and with scattering-induced broadening ($\sigma_0^2(z) = \sigma_0^2 \sqrt{1 + a_s n_0(z)}$). Panels **c**-**f** show the extracted fit parameters $\{\phi_-, A, C, \sigma\}$ without (red) and with interaction broadening. The black solid (dashed) line in panel **c** is the input relative (common) phase. From this figure, we observe that scattering-induced broadening does not significantly impact the extracted fit parameters except the width.
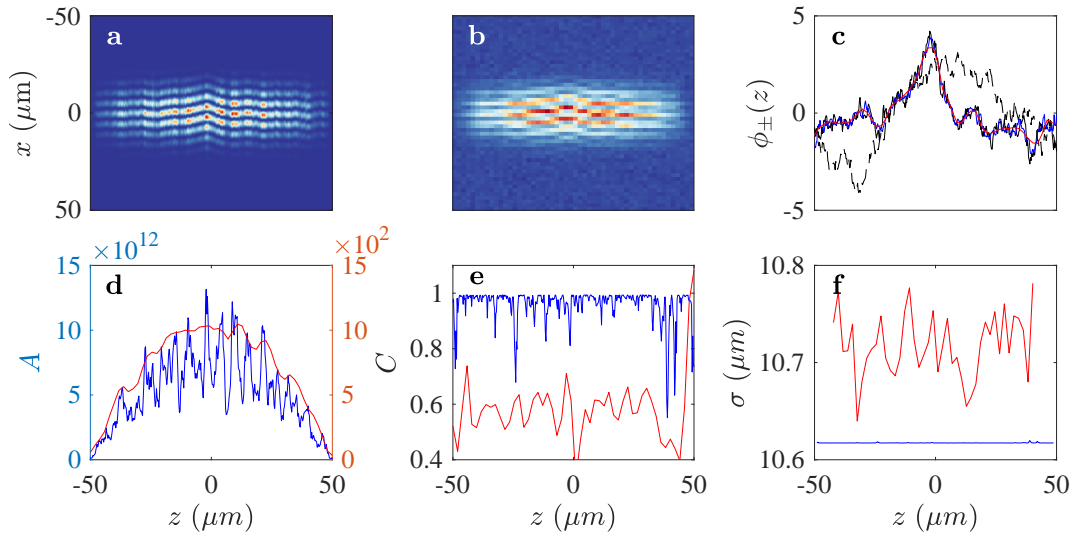
Figure 16: Single shot relative phase extraction with (red) and without (blue) image processing, similar to that of Figure 13 but for a short time-of-flight $t = 3.5$ ms. The common phase is denoted by a dashed line in panel **c**.
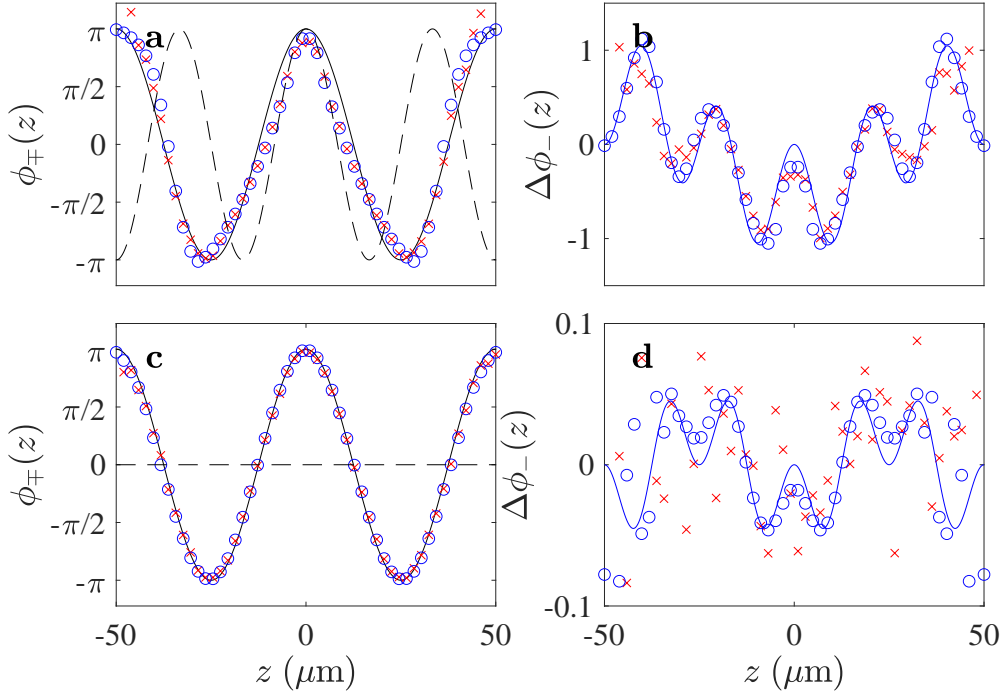
Figure 17: Simulation of analytic systematic phase shift before (blue) and after (red) image processing for 15 ms expansion time, see Fig. 3 for comparison.
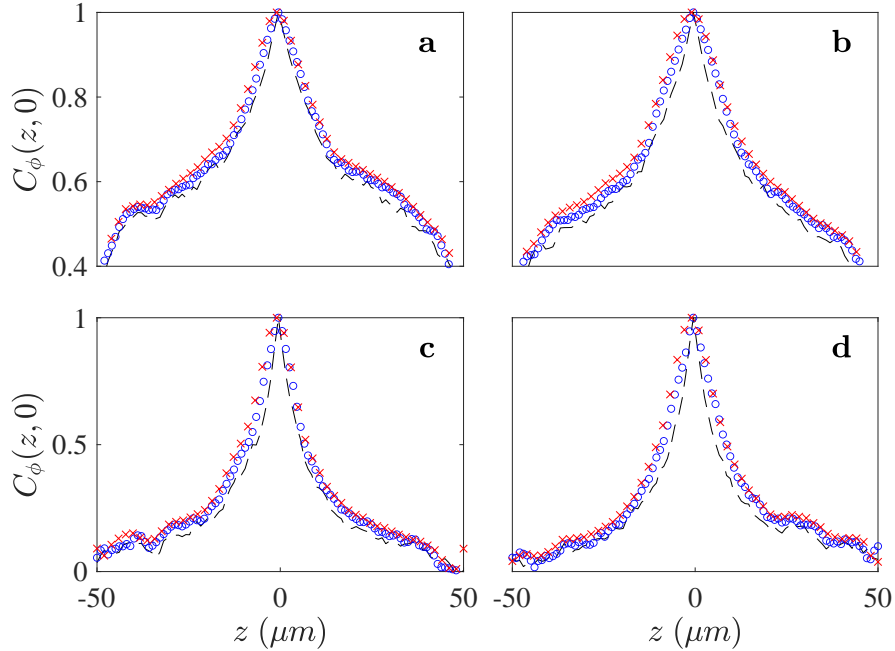

Figure 18: Phase correlation function C_ϕ with (red crosses) and without (blue circles) image processing. Each panel corresponds to the same parameter regime and number of shots as in Fig. 5 except that the common phase is always sampled from a thermal state with $T_+ = T_-$. The statistics are obtained with the camera defocusing set to 0 (ignoring recoil and free falling of the cloud during exposure), but we expect defocusing effect to be small.
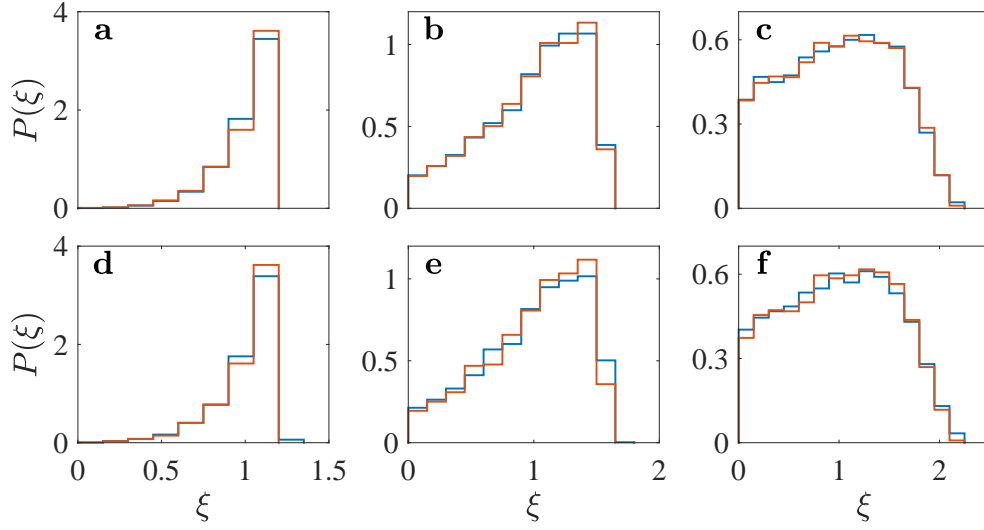
Figure 19: Full distribution function $P(\xi)$ before (blue) and after (red) image processing reconstructed with 5000 TOF simulations. Each panel correspond to the same parameter regime as Fig. 6 except for a fixed expansion time $t = 15$ ms. The statistics are obtained with the camera defocusing set to 0 (ignoring recoil and free falling of the cloud during exposure), but we expect defocusing effect to be small.
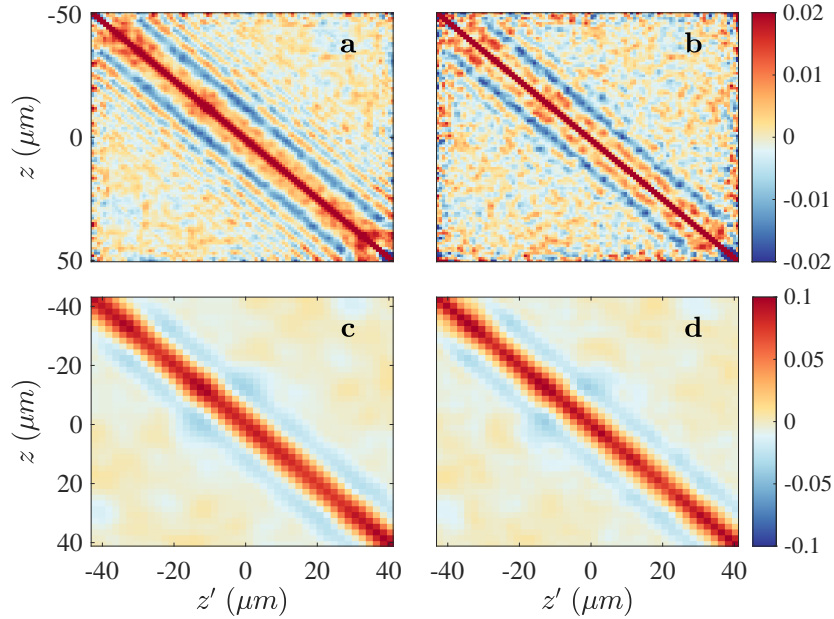

Figure 20: Velocity-velocity correlation $C_u(z, z')$ without (**a-b**) and with (**c-d**) image processing. The first column (**a**, **c**) corresponds to the case with $\phi_+(z) = 0$ and the second column (**b**, **d**) corresponds to the case with common phase sampled from the same thermal distribution as the relative phase $T_+ = T_- = 75$ nK. After processing, the correlation near the boundary is excluded due to artefacts from image processing. The statistics are obtained with the camera defocusing set to 0 (ignoring recoil and free falling of the cloud during exposure), but we expect defocusing effect to be small. The edge data of length 5 μm on each end have been omitted to suppress boundary effects.
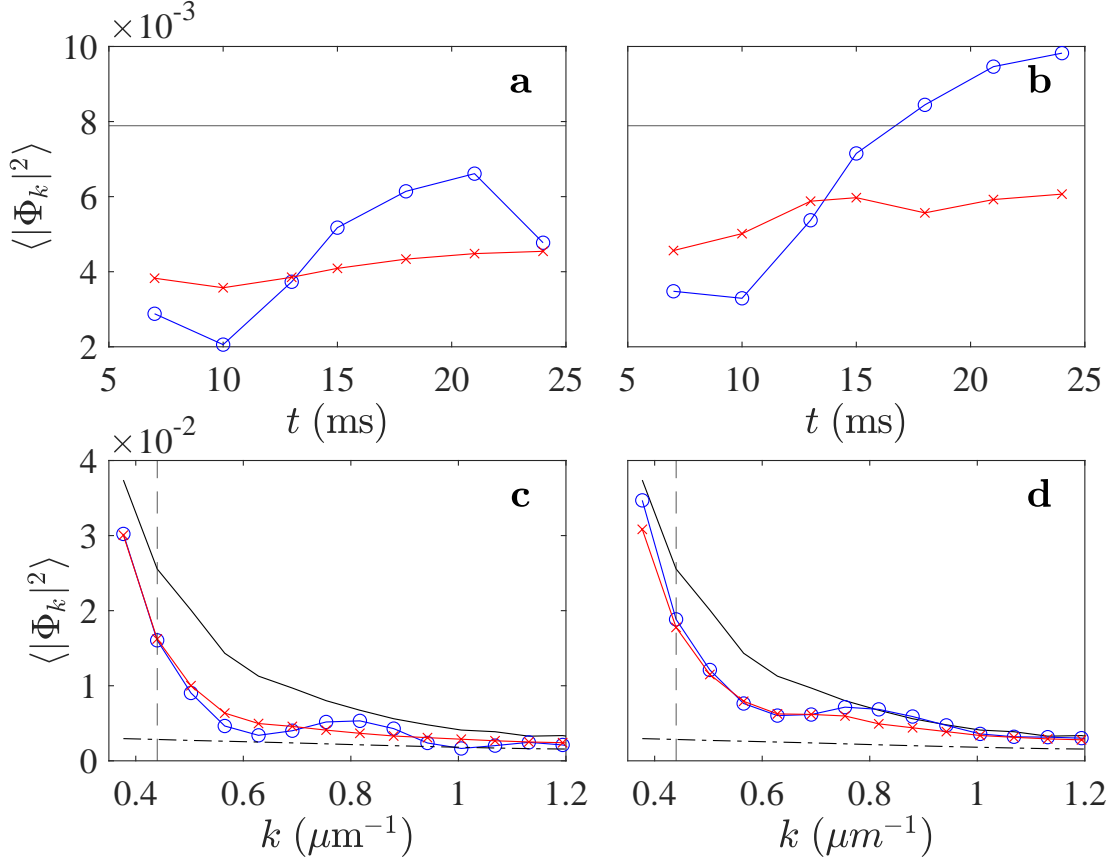
Figure 21: TOF reconstruction of mean Fourier mode (solid black line) before (blue circles) and after (red crosses) image processing computed with 500 TOF simulations for $T_- = 75$ nK. The solid black line represents the input value(s). In panels (**a**)-(**b**), the mode is fixed at $k = 22\pi/L \approx 0.69\ \mu m^{-1}$ while the expansion time t is varied. In **c-d** t is fixed at 15 ms but k is varied. The dashed vertical line at $k \approx 0.44\ \mu m^{-1}$ indicates the point where deviation due to image processing is apparent. The horizontal dashed-dot line shows the shot-noise fluctuations computed with TOF simulations of $\phi_-(z) = 0$. The first column (**a,c**) is for the case with $\phi_+(z) = 0$, the second column (**b,d**) is for the case with common phase sampled from thermal state with $T_+ = T_-$. The statistics are obtained with camera defocusing set to 0 (ignoring recoil and free falling of the cloud during exposure), but we expect the defocusing effect to be small.
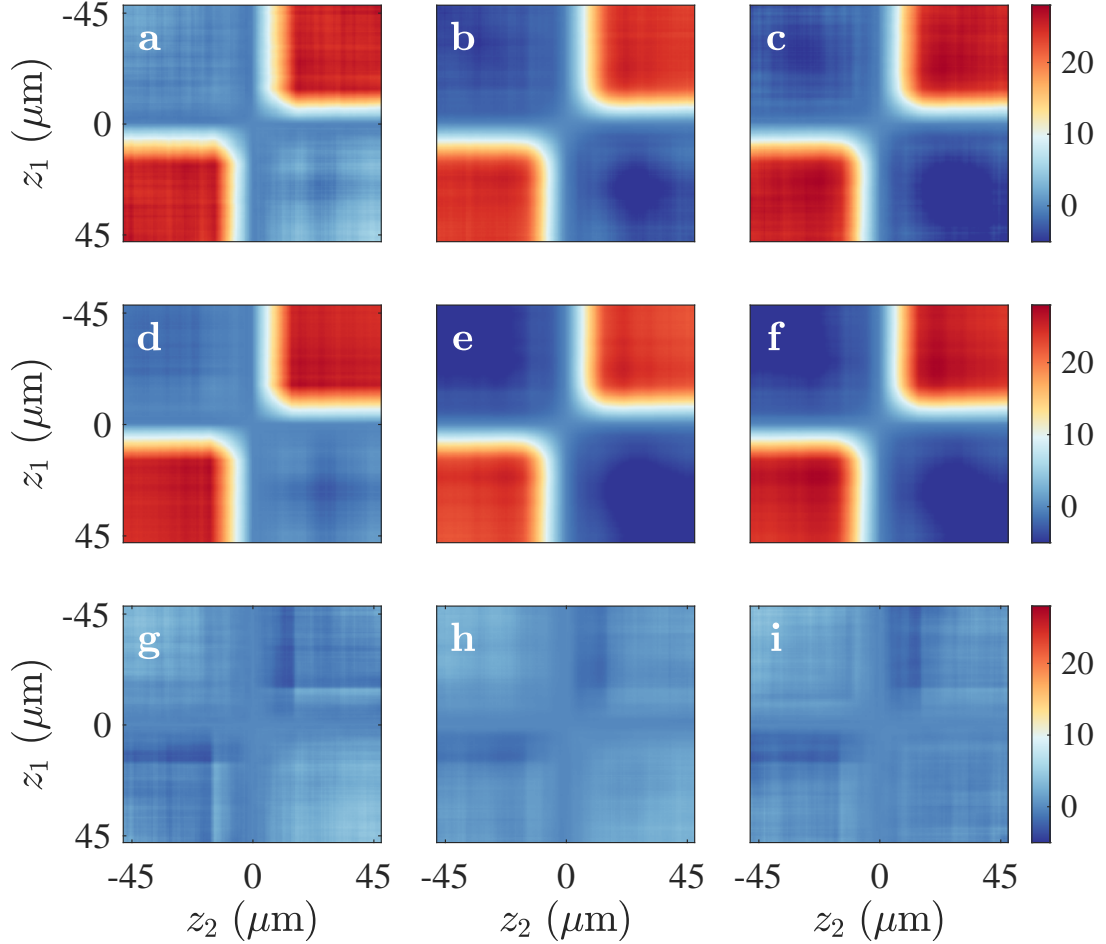
Figure 22: Time of flight (TOF) reconstruction of fourth-order correlation function $G^{(4)}(z_1, z_2, z_3, z_4)$ of the sine-Gordon model in the Gaussian regime ($q = \lambda_T/l_J = 0.5$). The data is cut at $z_3 = -z_4 = 15$ μm for visualization. Panels (**a-c**) show the full correlation, panels (**d - f**) show the disconnected part, and panels (**g - i**) shows the connected part. The first column (**a, d, g**) represents the case with only transversal expansion, the second column (**b, e, h**) includes longitudinal expansion but with common phase kept at zero and the last column (**c, f, i**) corresponds to the case with longitudinal expansion and common phase sampled from thermal distribution with $T_+ = 75$ nK. Each panel is reconstructed from 2500 TOF realizations with 15 ms expansion time. The edge data of length 2.5 μm on each end have been omitted to suppress boundary effects.